Tracking counterpart signatures in Saturn's auroras and ENA imagery during large-scale plasma injection events

J. Kinrade[1,4], S. V. Badman[1], C. Paranicas[2], D. G. Mitchell[2], C. S. Arridge[1], R. L. Gray[1], A. Bader[1], G. Provan[3], S. W. H. Cowley[3], C. J. Martin[1], N. Achilleos[5]

[1] Lancaster University, UK
[2] John Hopkins University Applied Physics Laboratory, USA
[3] University of Leicester, UK
[4] South African National Space Agency, SA
[5] University College London, UK

Corresponding author: Joe Kinrade (j.kinrade@lancaster.ac.uk)

Key points:

- Rotating enhancements in Saturn's morning auroras do not always have a counterpart in ENA emissions from the magnetosphere.
- Counterpart signatures can maintain a near 1:1 local time mapping throughout at least a planetary rotation.
- Remote sensing imagery, in conjunction with magnetic field mapping models, could provide characterisation of plasma flow boundaries.

Abstract

Saturn's morning-side auroras consist mainly of rotating, transient emission patches, following periodic reconnection activity in the magnetotail. Simultaneous responses in global energetic neutral atom (ENA) emissions have been observed in the same local time sector, hinting at a link between the auroras and large-scale injections of hot ions in the outer magnetosphere. In this study, we observe multiple plasma injection signatures within coincident auroral and ENA imagery captured by Cassini during 9 April 2014. Kilometric radio emissions also indicate clear injection activity. We track the motion of rotating signatures in the auroras and ENAs to test their local time relationship. Two signatures - separated by ~8 h UT - form in the auroras post-midnight and rotate around to the dayside while moving equatorward. The first has a clear rotating counterpart in the ENA emission, maintaining a similar local time mapping throughout ~9 h of observation. The second auroral signature has no clear ENA counterpart. Equatorward motion of the first auroral signature as it approaches the dayside implies a slowing down of the radial speed of the source region in the magnetosphere at a distance of ~14-20 R_S, suggesting a plasma or magnetic boundary. A third, older injection signature is seen in both the auroral and ENA imagery. This auroral patch may have been sustained by field-aligned currents linked with the southern PPO system, or a process driving re-energization of ENA patches around midnight local times. The ENA injection signatures form near magnetic longitude sectors associated with thinning of the magnetotail.

1 Introduction

Saturn's icy moon Enceladus ejects between tens to hundreds of kg of water-group molecules each second [e.g. *Jurac et al.*, 2002; *Jurac & Richardson*, 2005; *Burger et al.*, 2007]. Ionisation processes within the resulting neutral cloud continuously mass-load the inner magnetospheric field with plasma (e.g. *Bagenal & Delamere* [2011]). On average a steady-state system is maintained by shedding this plasma via radial transport processes, shifting the plasma from the inner magnetosphere to the outer magnetosphere where it is eventually shed from the system (e.g. *Thomsen et al.* [2013]). Radial transport between the inner and outer magnetosphere is controlled by an interchange instability, whereby cold, dense plasma is driven centrifugally outwards. Conservation of magnetic flux then requires more localized tenuous plasma to move rapidly inwards, forming filamentary radial hot plasma flows, referred to as interchange injections [e.g. *Burch et al.*, 2005, *Mauk et al.*, 2005, *Chen & Hill*, 2008; *Thomsen et al.*, 2015]. To finally remove the plasma from the system, magnetic reconnection in the outer magnetosphere, typically the magnetotail, results in the ejection of plasmoids [*Vasyliunas*, 1983, *Hill et al.*, 2008, *McAndrews et al.*, 2009, *Jackman et al.*, 2011; 2014, *Smith et al.*, 2016, *Arridge et al.*, 2016]. Recent work by *Guo et al.* [2018] shows that dayside magnetodisc reconnection may also play an important role in Saturn's global plasma transport.

Azimuthal flows dominate the global convection pattern out into the outer magnetosphere, beyond 20-30 Saturn radii, R_S, so these radial transport processes are superimposed on this background convection pattern [e.g. *Hill*, 1979, *Kane et al.*, 2008, *McAndrews et al.*, 2009, *Thomsen et al.*, 2010; 2014]. Global convection patterns are also constricted by the local time asymmetry imposed by the solar wind interaction [e.g. *Cowley et al.*, 2004; 2005, *Kellett et al.*, 2011], and are modulated by the periodicity so characteristic of Saturn's magnetosphere [e.g. see *Carbary & Mitchell*, 2013, *Kennelly et al.*, 2013].

Critically, a small fraction of the plasma in the magnetotail is not ejected from the system following reconnection. As the stretched field returns to a more dipolar state, hot plasma is accelerated planetward to the outer and middle magnetosphere in the post-midnight and morning local time sectors [e.g. *Mitchell et al.*, 2005, *Müller et al.*, 2010]. At Saturn, these events are referred to as large-scale hot plasma injections. *Thomsen et al.* [2015] suggest that the inward-moving injected hot plasma, when superposed with the bulk azimuthal plasma flow, may eventually encompass the cold, inner magnetosphere plasma throughout a wide local time range, setting up a plasmapause-like density gradient observed in particle measurements in as far as L = 8.6. Therefore, large-scale injections may be important triggers for subsequent small-scale plasma interchange injections [e.g. *Azari et al.*, 2018]. Note that the term 'plasmapause' at Saturn, according to *Thomsen et al.* [2015], represents the transition between hot, outer magnetosphere plasma and cold, inner magnetosphere plasma; separating the drift trajectories that close around the planet without experiencing tail reconnection or mass loss, from those that do encounter the reconnection region.

At this point it's useful to list some motivating questions. Can large-scale injections destabilize the plasma and enhance the number of small-scale injections? How far in do large-scale injections persist? To a plasmapause-like or magnetic pressure boundary? Can we see this boundary, if not the flow channels, using remote sensing observations?

What do we know from in-situ measurements and surveys? From the first orbits of Cassini, evidence of inward transport flow channels was found in the form of hot electron and ion injections [e.g. *Hill et al.*, 2004, *Burch et al.*, 2004, *Rymer et al.*, 2009, *Paranicas et al.*, 2010], with energy dispersion signatures indicating that these channels evolve in time [e.g. *Mauk et al.*, 2005, *Chen & Hill*, 2008, *Paranicas et al.*, 2016]. Over the lifetime of the Cassini mission, these flow channels have been observed to be ordered by both local time and global periodicities. Surveys of different datasets have demonstrated that interchange signatures are more often seen on the nightside than the dayside [*Kennelly et al.*, 2013, *Azari et al.*, 2018]. This local time dependency has been attributed to day/night variations in ionospheric conductivity affecting the growth rate of the interchange instability [e.g. *Southwood & Kivelson*, 1989; *Kivelson & Jia*, 2014]. The lack of a magnetopause on the nightside might also make it easier for cold plasma to move outward [e.g. *Kivelson & Southwood*, 2005]. Interchange injection signatures have been observed at radial distances between at least 5 and 11 R_S, but their frequency peaks around 6-9 R_S [e.g. *Chen & Hill*, 2008, *Thomsen*, 2013, *Paranicas et al.*, 2010, *Azari et al.*, 2018], coincident with the turnover in flux-tube content near 8 R_S [e.g. *Chen et al.*, 2010] and the plasmapause-like boundary discussed by *Young et al.* [2005] and *Thomsen et al.* [2015]. The plasmapause reported on the night-side by *Thomsen et al.* [2015] was detected at L = 8.6 during a fast, inclined orbit pass from the lobes into the closed field region, which (as those authors stated) would map equatorially to reconnection sites at distances >~15 R_S, and at local times within the distended tail region. Kennelly et al. [2013] also showed that the occurrence of injection signatures on the nightside is rotationally modulated by the SKR-derived Saturn longitude system (SLS), and this modulation has a seasonal dependence, further suggesting a connection to changes in ionospheric conductivity, or a change in the attack angle of the solar wind [e.g. *Arridge et al.*, 2008].

In situ observations allow a characterisation of the detailed structure within injections, to examine the physical processes at work, and to examine the drivers for transport (e.g., the characterisation of flux tube content profiles and pressure gradients). Through surveys, in situ data can reveal glimpses of global-scale convection patterns, but are naturally biased by the trajectory of the spacecraft, sampling resolution, and instrument fields of view.
In contrast, remote sensing can provide a more time coherent, holistic view of large-scale plasma morphology than can be obtained from in situ spacecraft measurements. For example, auroral imaging can provide a morphological view of the wider system dynamics, at the expense of a

detailed understanding of the plasma properties and behaviour. Instead, we observe markers or proxies for the physical processes as they manifest in, for example, auroral emissions in the ionosphere. Auroras can indicate where in the magnetosphere plasma dynamics are happening, and how they are evolving. Their morphology can tell us about the system response to solar wind driving [e.g. *Badman et al.*, 2013, *Nichols et al.*, 2014]. Emission intensity and spectral information can provide some inferences about the source plasma and acceleration processes [e.g. *Gustin et al.*, 2009], and the strength of the upward field-aligned current systems (such as those associated with the planetary period oscillations) [e.g. *Bader et al., 2018*].

In this study we use observations of auroral emissions and energetic neutral atoms (ENA) as remote indicators of magnetospheric dynamics. Saturn's extended neutral cloud makes it an efficient ENA emitter [e.g. *Brandt et al.*, 2018]. Following collisional charge exchange with the neutrals, energetic ion injections manifest as discrete regions of enhanced ENA intensity, visible in the line-of-sight integral flux images taken by the ion-neutral camera (INCA). ENAs are useful because they carry information about the original ion's energy and trajectory, but the interpretation of such integral-based images is highly dependent on spacecraft viewing geometry [e.g. *Paranicas et al.*, 2005].

Large-scale plasma injections are regularly observed in ENA imagery [e.g. *Mitchell et al.*, 2005; 2009, *Carbary & Mitchell*, 2014]. *Mitchell et al.* [2005] and *Hill et al.* [2008] first attributed sudden ENA brightening events to the presence of accelerated ion return flows reaching the inner magnetosphere. In statistical morphologies, peak ENA flux occurs broadly around midnight local times [e.g. *Carbary et al.*, 2008]. There is evidence that reconnection activity and magnetic field dipolarization signatures in the magnetotail are modulated by planetary-period thickening and thinning of the tail [*Jackman et al.*, 2016, *Cowley et al.*, 2017, *Thomsen et al.*, 2017, *Bradley et al.*, 2018]. Recurrent ENA energizations and statistically significant periodicity in global ENA flux images at near-planetary period also hint at this modulation [e.g. *Carbary et al., 2008*, *Paranicas et al.*, 2005, *Krimigis et al.*, 2005]. *Mitchell et al.* [2015] showed that large-scale injection ENA signatures can appear recurrently in the absence of strong solar wind driving, further suggesting that the associated tail reconnection activity is mainly modulated by internal planetary-period processes (although tail instabilities leading to reconnection can still be triggered by solar wind compressions [e.g. *Bunce et al.*, 2005]).

We focus on signatures in Saturn's ultraviolet (UV) auroras. Most pertinent to this study, auroral signatures have been associated with large-scale plasma injection events, appearing to broadly follow the local time position of ENA emission signatures as they rotate around the planet [e.g. *Mitchell et al.*, 2009, *Lamy et al.*, 2013, *Nichols et al.*, 2014]. These auroral 'spots' or 'patches' first appear poleward of the main emission on the nightside of the planet in response to dipolarization of the stretched magnetotail field following reconnection [*Jackman et al.*, 2013]. Equatorward bifurcations from the main auroral emission at later local times may also map to areas of active interchange in the magnetosphere, triggered as the source region plasma drifts inwards and disperses [e.g. *Radioti et al.*, 2013]. A recent survey of Cassini Ultraviolet Imaging Spectrograph (UVIS) data has confirmed that Saturn's dawn-side auroras are dominated by bright, transient features rotating through the sector, likely following large-scale injection events [*Bader et al.*, 2019b].

The exact nature of the transient current system linking these rotating ENA and auroral signatures remains an open question. A few schools of thought exist; pressure-driven currents around the edges of injections requiring closure in the ionosphere [*Mitchell et al.*, 2009; *Brandt et al.*, 2018, *Nichols et al.*, 2014]; plasma heating driving wave-particle scattering [*Radioti et al.*, 2013]; an ionospheric resistance to a moving plasma bubble once it reaches a limiting entropy at some radial boundary [e.g. *Wolf et al.*, 2009, and references therein]; or regions of filamentary current flows

related to interchanging flux tubes [*Lamy et al.*, 2013]. Regarding the plasma bubble theory, in the magnetosphere it is believed that the injected plasma population is stopped near the location where the entropy inside the injection equals the entropy outside it. On a microscopic scale, the particles in the hot plasma move inward under the influence of a radial E × B drift, and this E field must map along the magnetic field lines from the inward plasma flow channel to the ionosphere, which would attempt to impede the inward motion of the distribution [e.g. *Rymer et al.*, 2009]. Any plausible link between auroral emissions and ENA enhancements must account for the auroral signature being a proxy for electron precipitation, while the ENA signature is a proxy for ion loss processes. An open question is how do these systems evolve in time? Are they always counterpart? Do auroral signatures persist for as long as the ENA enhancements? How do energy-dependent particle drifts, which tend to spatially disperse inward-moving plasma injections, affect the local time relationship?

Inspired by these questions, in this paper we present a case study, using partially coincident auroral and ENA images captured during a southern high latitude Cassini orbit on 9 April 2014, in which three injection signatures are observed at various stages of development. We track the location and extents of these injection signatures in the auroral and ENA images to test if they are counterpart. Beyond the interval of ENA and UV observations, ongoing SKR emissions also indicate significant injection activity throughout the day. Section 2 introduces the Cassini remote sensing data. Image analysis methods are described in section 3, including keogram construction and tracking the motion of both ENA and auroral patches. In section 4 we examine the local time conjugacy of rotating signatures in the auroral and ENA responses, and test for coincident low frequency extensions in the SKR emission. We discuss the interpretation of these rotating signatures as indicators of possible injection activity, and surmise that their occurrence is likely modulated by periodic reconnection processes in the magnetotail.

2 Data & Methods

This study draws on observations from three of Cassini's instruments, made throughout day 2014-099 (9 April 2014). We analyse auroral imagery from the Ultraviolet Imaging Spectrograph (UVIS) [*Esposito et al.*, 2004], ENA imagery from the Ion-Neutral Camera (INCA) [*Krimigis et al.*, 2004], and radio spectrometer data from the Radio and Plasma Wave Science (RPWS) instrument [*Gurnett et al.*, 2004]. The spacecraft was positioned in the southern hemisphere on an inclined orbit ('Rev 203'), providing wide-area views of the southern auroras (observed by UVIS) and morning-sector magnetosphere (observed by INCA). Cassini was orbiting at distances of ~12-5-13.5 R_S from the planet throughout the INCA observation window, moving around the post-noon - dusk sector from ~15 LT to ~19 LT. Latitude increased from -31° at the start of the day, to -41° by the end of the INCA window (~1930 UT). (Detailed orbit information can be seen in the additional axes of Figure 5). Here we briefly discuss the data and their limitations.

2.1 Cassini UVIS

Auroral images were obtained using the far ultraviolet (FUV) channel of UVIS, the 110-190 nm waveband capturing Saturn's most powerful auroral emissions. Wide-area pseudo-images of the auroral region may be constructed by successively slewing the sensor across the planet from high latitude orbit positions. Since the FUV passband includes emission wavelengths affected by atmospheric hydrocarbon absorption, the measured spectral intensity between 155.5-162.0 nm (unattenuated by absorption) is integrated and multiplied by a factor 8.1 (as determined from a synthetic H_2 spectrum) to reproduce the total unabsorbed H_2 emission intensity in the full 70-170

nm range [e.g. *Gustin et al.*, 2017]. As the south was the winter hemisphere in 2014, no background intensity subtraction was necessary (i.e. the auroral emissions were superposed on a planet background which was negligible since that part of the planet was in darkness). Resulting intensity values are mapped to a 0.25° x 0.5° latitude-longitude grid by projecting the pixels onto an ellipsoid at an altitude of ~1100 km (above Saturn's 1-bar pressure surface), characteristic of Saturn's peak auroral emission [*Gérard et al.*, 2009]. On-planet pixel size therefore varies across the slew and along the slit.

The UVIS sensor consists of 64 spatial × 1024 spectral pixels, with each spatial pixel having an angular resolution of 1.0 x 1.5 mrad. Spacecraft distance and relative latitude-longitude on the surface determine the effective spatial resolution on the planet, which in this case was ~750 km for a sub-spacecraft pixel. The images used in this study have exposure times of ~60 mins or less (1-2 slews combined), during which the planet will have rotated by ~34° (or ~2.26 h LT, see section 2.5). This does not translate directly to a systematic spatial 'blur', as each spatial region is usually only covered once by the slit slewing i.e. the pseudo-images do not exhibit time coherency across all pixels within an exposure.

2.2 ENA imagery from the Cassini INCA

An ENA is created when a singly charged ion gains an electron from a neutral gas atom or molecule. The ENA's motion is no longer governed by the magnetic or electric fields, nor the gravitational field if it has enough energy. It then travels away from the charge exchange site on its original trajectory (as a former energetic ion), with most of its original energy. The ENA thus carries information about the source plasma and energy spectrum. Wide area remote sensing of ENAs can therefore act as a diagnostic of the global plasma dynamics of a magnetosphere, a technique first developed in imaging Earth's ring current plasma [e.g. *Roelof*, 1989].

Saturn has been described as a near-ideal ENA emitter [*Brandt et al.*, 2018], as most of the magnetospheric neutral density is confined to the equatorial plane, and its magnetic dipole axis is aligned with its spin axis. The extended neutral gas cloud therefore acts as a screen for revealing energetic ion injections. Additionally, radiation levels near the Cassini spacecraft are frequently very low in the middle-outer magnetosphere (due to Saturn having weak radiation belts at such distances) such that the effect of local energetic particles masking out remote neutral atom detections is minimal. Remote sensing of the ENA emission from high above the poles can provide information about the wide-area plasma dynamics at all local times. Equatorial grid projections of the ENA images from suitable high-latitude orbit positions are commonly used for imaging azimuthal asymmetries (associated with partial ring current morphologies) and rotating injection signatures [e.g. *Brandt et al.*, 2008, *Lamy et al.*, 2013, *Carbary & Mitchell*, 2014].

INCA is a time-of-flight instrument that detects ENAs in several energy pass-bands, discriminating hydrogen and oxygen by their secondary electron scatter profiles on its charge plates. The instrument field of view is 120° x 90°, with spatial grid resolution up to 64 x 64 pixels, depending on the energy resolution. Image integrations are built up as the spacecraft orbits and are constructed by the standard pipeline processing [*Krimigis et al.*, 2004]. We chose to preserve the native 64 x 64-pixel resolution of the INCA, rather than apply the boxcar-smoothed images typically used in other studies, before projecting the images into Saturn's equatorial plane. Keograms were then constructed from local time versus radial distance profiles of the median differential ENA flux, calculated every 1° of azimuth around Saturn, and out to a magnetospheric distance limit of 20.7 R_S.

This distance limit was chosen as the statistical standoff distance of the dayside magnetopause in its compressed mode [*Achilleos et al.*, 2008, *Pilkington et al.*, 2015], and it is close to Titan's orbit – the point at which ENA injection signatures first begin to manifest as the incoming ions meet larger neutral density gradients [e.g. *Carbary et al.*, 2008]. Equatorial projection validity also falls off with distance from the spacecraft as the inclination angle becomes more oblique (i.e. as the spacecraft approaches the equator), and projected pixels become stretched at certain local times. On day 2014-099 the Cassini INCA was viewing almost the entire dawn sector from a dusk position. The projected INCA grid pixels most distant from the spacecraft (in the morning sector) span up to ~10 R_S radially but are only ~1-2 R_S in the azimuthal direction. Hence the ENA keograms presented here mainly reveal the azimuthal variation of ENA flux in time.

The ENA flux, ξ_{ENA}, detected by the INCA at energy *E,* is measured as a line-of-sight integral of the ion flux, ξ_{ION}, neutral density, *n*, and charge exchange cross section, σ, along path l [e.g. *Brandt et al.*, 2005]:

$$\xi_{ENA}(E) = \int_0^\infty \xi_{ION}(E,l)n(l)\sigma(E)dl \qquad (1)$$

This expression shows that the ENA image intensity is not just a function of the ion intensity, but is a convolution with the neutral column density along the line-of-sight. ENA images in this study show the differential ENA flux, being the number of ENAs per unit area per solid angle per unit time per unit energy (counts / cm^2-sr-s-keV). Hydrogen images have higher effective resolution than oxygen images for a given energy due to relative scatter levels in the front foil of the INCA [*Brandt et al.*, 2005]; here we analyse H imagery in the energy range 24-55 keV, in high-spatial resolution neutral mode. The equatorial projections of the INCA images used for this study are provided in Supporting Information S1.

2.3 Cassini RPWS

We include a radio frequency spectrogram from the Cassini RPWS instrument throughout day 2014-099, which provides context for possible auroral and large-scale plasma injection activity in the Saturn Kilometric Radiation (SKR) frequency range. SKR typically peaks between 100-400 kHz (but can range between 3 kHz to 1.2 MHz), and is closely related to auroral acceleration processes [e.g. *Lamy et al.*, 2008, 2009]. Periodic modulation of the SKR emission, as observed by the Voyager, Ulysses and (more extensively) Cassini missions, has informed our definition of Saturn's complex rotation periods in each hemisphere (the length of a day on Saturn is still a matter of discourse). In general terms, the SKR emission power intensifies periodically as a source region passes through the morning side of the planet [*Lamy et al.,* 2009]. But this periodicity is independent in each hemisphere [e.g. *Gurnett et al.,* 2009], changes with Kronian season [e.g. *Galopeau & Lecacheux*, 2000, *Cowley & Provan,* 2016], and can be interrupted by solar wind shock fronts impacting the magnetosphere [e.g. *Badman et al.,* 2008]. This results in a mix of modulation periods emergent in statistical studies [e.g. *Zarka et al.,* 2007, *Jackman et al.,* 2009, *Reed et al.,* 2018]. We refer the reader to the concise introductory review within the study of *Reed et al.* [2018, and references therein] for further background on the SKR emission, its production and interpretation.

In terms of auroral and injection activity, of interest here are the low-frequency extensions (LFEs) of the SKR emission. LFEs are marked intensifications of the main emission power, together with expansion of the emission to lower frequencies (tens of kHz). *Jackman et al.* [2009] characterised LFEs, associating them with extension of the auroral acceleration region to higher altitudes along magnetic field lines, in response to field-aligned current reconfiguration after reconnection in the magnetotail. Using a catalogue of magnetic reconnection signatures constructed by *Smith et al.*

[2016], an extensive SKR survey by *Reed et al.* [2018] has since confirmed that 'short' LFE events lasting < 20 h are a good proxy indicator of magnetotail reconnection; 60% of detected LFEs occurred within 6 h of a preceding tail reconnection signature. Hence, in searching for large-scale injection signatures in the auroral and ENA emission, we may look to the global SKR emission for their precursor – reconnection activity in the magnetotail.

Since we are observing Saturn's southern hemisphere auroras, we use the left-hand circular polarised (LHCP) power measurements. These measurements are normalised for spacecraft distance and corrected for interference artefacts as described in *Lamy et al.* [2008]. These data are available from http://www.lesia.obspm.fr/kronos/.

2.4 Ionosphere-magnetosphere mapping profiles

In comparing auroral and ENA imagery, it is useful to know at which distances the auroral emission regions map to in the magnetosphere. To estimate this, we use ionosphere-magnetodisc mapping profiles based on an offset symmetric dipole model plus a semi-empirical model of the current sheet [*Achilleos et al.*, 2008, *Sorba et al.*, 2018]. Adjustable parameters include the magnetopause stand-off distance and 'ring current activity', the latter being based on statistical hot plasma pressure profiles from in-situ Cassini measurements [*Sergis et al.*, 2009]. The model provides ionospheric mapping profiles based on the state of compression or expansion of the magnetosphere. Note this transform is in the radial direction only, taking no account of azimuthal bend back or bend forward of the field. We take the statistical bimodal magnetopause stand-off distances for a compressed (20.7 R_S) and expanded (27.1 R_S) magnetosphere, based on the Cassini crossing surveys of *Achilleos et al.* [2008] and *Pilkington et al.* [2015]. Using the compressed (expanded) model, typical morning-sector auroral features at ~17° southern colatitude [*Bader et al.*, 2018] map to ~16 (22) R_S in the equatorial plane; this range gives an indication of the uncertainty in the ionosphere-magnetosphere mapping, associated with variability in magnetospheric size.

A study by *Carbary et al.*, [2008] found that the average ENA morphology over a 120-day interval in 2007 mapped to locations in the ionosphere equatorward of and separate to the main auroral emission (using dayside-only boundaries determined from HST imagery by *Badman et al.* [2006]). Those authors also note, however, that the averaging process obscures the temporal behaviour of the ENA emissions, such that transient features are not accounted for across the local time range (i.e. those responsible for the main auroral emission, particularly at dawn [*Bader et al.*, 2019b]). Consider that the large-scale injection signatures in the ENA emission are typically brightest when they initialise around midnight, poleward of the main auroral latitudes, then dim as they subsequently move equatorward and into the main auroral latitudes as they rotate; this may explain the apparent mapping disparity in the average picture of *Carbary et al.* [2008]. Indeed, our results will show that transient, rotating ENA enhancements can map to auroral latitudes.

2.5 Rotating current systems and planetary rotation rate

The position and intensity of Saturn's auroras are known to be modulated by the rotating patterns of field aligned currents (FACs) imposed by the two planetary period oscillation (PPO) current systems [e.g. *Hunt et al.*, 2015, *Bader et al.*, 2018; 2019a]. The extent of this modulation depends on the relative phases, strengths and superposition of the north-south systems in each hemisphere, which changes slowly with time. During early-mid 2014, the two PPO systems settled into a period of coalescence, whereby they locked in anti-phase at a common period of ~ 10.69 h [*Provan et al.*, 2016]. This is equivalent to ~33.65° of longitude per hour (or ~2.24 h of local time per 1.00 h of universal time), a rate which we refer to here as the PPO corotation, Ω. In the southern hemisphere,

the region of primary upward field-aligned current associated with the PPO system model peaks at a PPO longitude of $\psi_S = 270°$, where auroral brightening may thus be expected. We use the latest available phase model values from the University of Leicester (see Acknowledgements).

The rotating north-south PPO perturbation fields superimpose in the magnetic equator and, particularly when in anti-phase, have been shown to modulate the thickness of the current sheet [e.g. *Provan et al.*, 2012, *Cowley et al.*, 2017, *Thomsen et al.*, 2017, *Bradley et al.*, 2018]. *Jackman et al.* [2016] also observed plasmoid occurrence in the magnetotail to be more likely under the same anti-phase conditions. The tail thinning effect associated with this modulation pattern maximizes at PPO longitudes $\Psi_S = 180°$ and $\Psi_N = 0°$, when reconnection in the tail (and therefore, possibly, ENA intensification) is statistically more likely [*Bradley et al.*, 2018]. Tail thickness modulation is therefore amplified when the north-south PPO systems superpose in anti-phase, as was the case in 2014 and the case we present here. Model phase values from *Provan et al.* [2016] were within ~20° of anti-phase throughout day 2014-099.

3 Observations

3.1 FUV auroral imagery

Figure 1 shows a sequence of UVIS polar-mapped projections showing the changing morphology of Saturn's southern auroras on day 2014-099. The sequence spans ~8.7 h between 0837-1736 UT. It is clear that the auroras were generally active and structured throughout, with emissions detected in all local time sectors. Image 1a exhibits multiple patches of emission across half the local time range between post-midnight and post-noon, distributed across a colatitude range of ~20° to ~5° colatitude. The dusk sector displays a series of less intense patches across a narrower colatitude band between ~15-23°, forming a near-continuous arc of emission between post-noon and midnight that shifts equatorward at later local times.

To quantify patch rotation speeds and intensity changes, we use a simple tracking method based on an emission intensity threshold. For each image, a contour value was taken as the 98^{th} percentile point of a smoothed (7×7-pixel boxcar filter) intensity distribution of all pixels within 30° colatitude of the pole. These contours are superimposed on the intensity maps of Figure 1 as white lines, essentially highlighting the brightest features in each image. Use of a relative dynamic intensity threshold maintains tracking of individual patches throughout the sequence regardless of overall brightness changes in the images. Boxes bound the maximum local time and latitude extents of each tracked patch, and crosses mark the centroid based on the contour. While this tracking method is not exact in picking out visible patch shapes as they appear to the eye, it is simple, systematic and repeatable. In Figure 1 we have shaded three possible auroral injection signatures to highlight their rotation throughout the sequence (non-shaded versions of the UVIS imagery are provided in the Supporting Information S2).

The sequence reveals the rotation of auroral patches around the planet as the morphology developed. See for example the patch in Figure 1a at ~03 local time (LT), which moves around to ~06 LT in 1c, and has almost reached noon by the time of 1f. From this point we label this feature 'U1' (green in Figure 1) for convenience, and subsequent rotating features are numbered in time order as they appear in UT. A rotating patch is also present in the nightside sector at first (U2, magenta), clearest in images 1c-f, moving from ~22-23 LT through midnight and then back around to dawn in 1g-i; note that U2 is only partially tracked in 1c-f, which is a limitation of the method described above. A second morning-sector patch appears on the poleward side of the main

emission just before 06 LT in 1f (U_3, orange), which then increases in size and intensity as it rotates through to noon by 1i. The radial black dashed line plotted in each panel of Figure 1 marks the local time position of maximum upward current expected from the southern PPO current system (Ψ_S = 270°at the central time of each UVIS exposure), giving a sense of planetary rotation speed. Using this line as reference, the azimuthal rotation speed of the auroral patches (essentially forming the entire morphology in this case) appears to lag behind rigid co-rotation throughout the sequence. There are other morphological features in the sequence aside from possible injection signatures, such as the multiple morning patches in 1a between 15-20° latitude, spaced by ~ 1 h LT, which appear similar to those associated by *Meredith et al.* [2013] with currents driven by ULF wave activity. We also note that the whole dayside sector appears to brighten towards the end of the sequence (1g-i), when a bifurcation feature (or equatorward 'split' away from the main emission latitudes) also develops post-noon at ~15 LT.

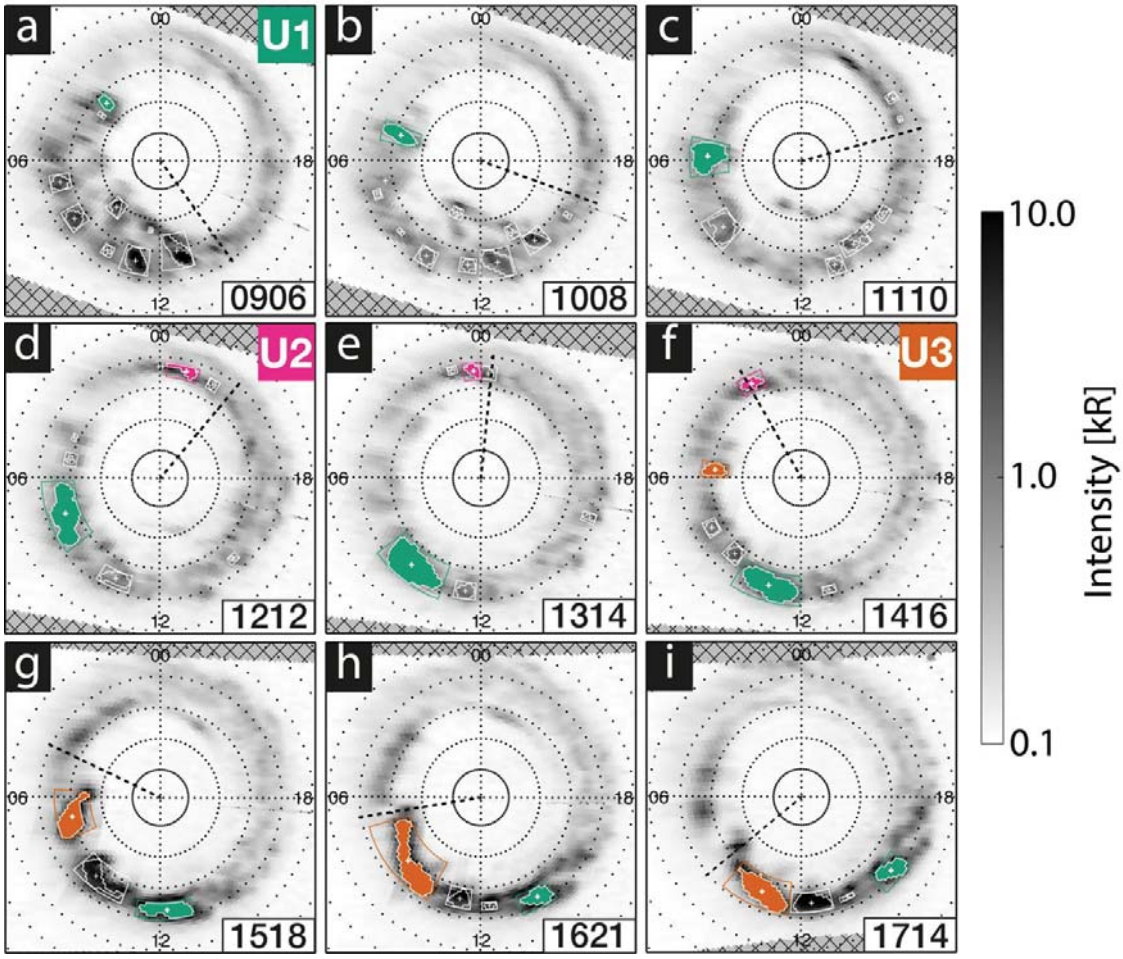

Figure 1. A sequence of 9 UVIS FUV pseudo-images in polar projection showing Saturn's southern auroras on day 2014-099. The sequence spans ~8.7 h from 0837 to 1736 UT. Images were taken in slew-mode with exposure times of ~ 60 mins (except the last image being ~ 44 mins), providing a view of the entire southern oval. Mid-exposure times are labelled. Local time is labelled at 00, 06, 12 and 18 LT, and black dots along these meridians have 1° latitude spacing. Rings of colatitude are shown by dots every 5° from the pole. Auroral patches are highlighted by white contours, which surround pixel areas with values above 98% of each image pixel-intensity distribution within 30° colatitude. White crosses mark patch centroids. Bounding boxes encompass the contour areas using the largest local time and colatitude extents of each patch. A black dashed line marks the

local time position of maximum upward current expected from the southern PPO current system i.e. $\Psi_S = 270°$. Three possible auroral injection signatures, labelled U1, U2 and U3 in order of appearance, are highlighted in green, magenta and orange, respectively.

Figure 2 details the motion of the three main patches described above (herein referred to as U1, U2 and U3), in local time (2a) and colatitude position (2b). Points plotted are the patch centroid position, and vertical bars show the extents of the associated contour bounding box in local time and colatitude (see boxes in Figure 1). Only patch U1 was tracked through all nine UVIS images. This patch rotated steadily through local times ~03-16 LT in ~8.7 h, which, based on a best line fit, equates to an azimuthal speed component of ~69% of the planet's PPO rotation rate during 2014 (see section 2.5).

Patch U1 also moved equatorwards throughout the sequence (implying an inward moving source region in the magnetosphere), from ~13-19° colatitude. There is a reduction in the rate of patch U1's equatorward motion between ~1143-1346 UT as it rotates towards local noon (Figure 1d-f), as indicated by the knee-point at ~18-19° centroid colatitude position in Figure 2b. Annotation shows the estimated radial speed of an inward moving auroral source region in the magnetosphere, based on these ionospheric colatitudes as they map out to the equatorial plane using the UCL magnetodisc mapping model (see Section 2.4). The lower and upper speed estimates relate to magnetopause standoff distances of 20.7 R_S and 27.1 R_S. The source region associated with patch U1 may therefore have slowed down upon reaching a distance of ~14-20 R_S, with radial inward speeds reducing by factor ~5-8 across this apparent boundary, from ~49 km s^{-1} to ~8 km s^{-1}. Simultaneously the brightness of patch U1 increased, as detailed in Figure 2c, which tracks the estimated mapping distance of the magnetospheric source region versus the intensity of the pixels within the patch. The mean intensity almost doubled from ~5 kR at ~7.5 LT to ~9 kR at ~12 LT; only increasing when the patch underwent braking of its inward motion between ~9-12 LT (Figure 2a shows that the azimuthal speed component was ~ unchanged). The same trend is evident with the maximum intensity values shown by red points. Before and after this braking point, the brightness of the patch generally decreased during times of steady inward motion.

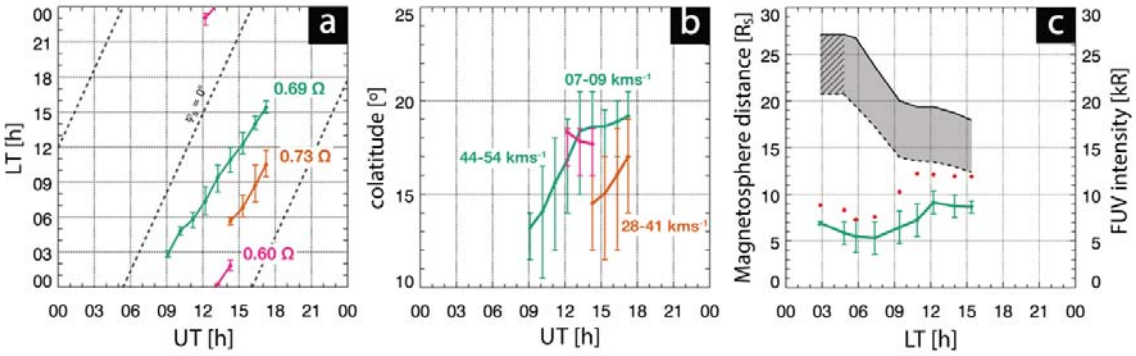

Figure 2. Local time (2a) and colatitude (2b) positions of the three clearest rotating auroral patches identified in the polar-projected UVIS imagery (shading color is consistent with patches U1, U2 and U3 in Figure 1). Annotation in 2a shows the approximate azimuthal speed of each patch based on a line of best fit, expressed as a fraction of PPO corotation (for clarity the PPO corotation gradient in this UT-LT frame is illustrated by a black dashed line at the LT position of the southern PPO dipole i.e. $\Psi_S = 0°$). Annotation in 2b indicates the inward radial speed of an auroral source region in the magnetosphere estimated by mapping the tracked auroral patch colatitudes. Upper and lower speed ranges correspond to typical compressed and expanded magnetosphere states. Vertical limit bars show the local time (2a) and colatitude extents (2b) of the patches detected in each image. (2c)

shows the tracked centroid position of U1 in local time versus estimated magnetospheric source distance in the equatorial plane. Gray shading indicates a region of possible mapping extent based on an inflated (solid black line) and compressed (dashed black line) magnetosphere (the hatched area shows where the colatitude value mapped to a distance beyond the mapping boundary, and upper limits are used instead). A secondary axis shows the mean (green line and mean absolute deviations) and maximum intensity (red dots) of the patch, based on all pixels within the contour boundaries highlighted in Figure 1.

The second auroral patch, U3, appears in Figure 1e (1245 UT) as a low-intensity feature (~3-5 kR) poleward of ~15° colatitude between ~04-06 LT. This location is similar to that of patch U1 ~4 hours earlier. Patch U3 is only picked up automatically in Figure 1f, when it brightened to > 10 kR pre-dawn. The evolution of U3 then resembles that of U1, moving equatorward and around to the dayside with similar azimuthal (0.73 Ω) and radial speeds (27-30 km s^{-1}), brightening and spreading in local time. The UVIS sequence did not capture U3 subsequently moving through noon, but by this time the patch was contributing to an apparent brightening of almost the entire dayside sector (see Figure 1h-i).

Patch U2 is highlighted in magenta in Figure 1d-f and traces in Figure 2. U2 differs from U1 and U3 in that it is first visible in the pre-midnight sector, between ~22-23 LT and colatitudes of ~18-19° (Figure 1c). The tracking procedure then picks up this patch in Figures 1d-f as it moved through local midnight and brightened to > 10 kR at ~02 LT (Figure 1f), with azimuthal speed ~0.60 Ω (Figure 2a). Patch U2 then dimmed again but continued to rotate through to the dawn sector, forming part of the morning sector arc between ~03-06 LT and ~14-19° colatitude (Figure 1h). Figure 1h shows a clear gap of ~5° colatitude in the morning sector morphology at ~06 LT, which is formed by the remnants of patch U2 (pre-dawn) and U3 (post-dawn). We interpret U2 as a signature of an older injection event, preceding those associated with patches U1 and U3, having completed a rotation about the planet. As expected the intensification of patch U2 around midnight is coincident with the region of expected upward PPO current as it passes through the same broad local time sector. We omit a radial speed estimate for U2 in Figure 2b, as the magnetospheric mapping is less valid in the stretched magnetotail region on the nightside (see Section 2.4).

Figure 3 shows an auroral keogram, plotted in the same UT-LT frame as Figure 2a, showing local time profiles of the maximum intensity values in each UVIS image between 0-30° colatitude. The width of each pixel column indicates the total exposure time of the image. In this keogram, regions of enhanced intensity with positive gradient (aligned diagonally in the UT-LT frame) indicate auroral patches rotating around the planet, their gradient indicating azimuthal speed. The effective time resolution of ~1 h provided by the slew-mode images makes accurate patch tracking in this frame difficult (although rotating features are visible), so we have overlaid the centroid tracks of patches U1 (green), U2 (magenta) and U3 (orange) to guide the eye. The keogram in this case simply provides another way of visualizing the time evolution of the auroral morphology shown in Figure 1, particularly the rotating patches. We include it here for comparison with the ENA flux distribution described in the next section (white hash contour-shading here in Figure 3 is an overlay based on Figure 4), as the equatorial projections from INCA lack the radial resolution required to isolate and track individual patches using a contour threshold, and a keogram must be used instead.

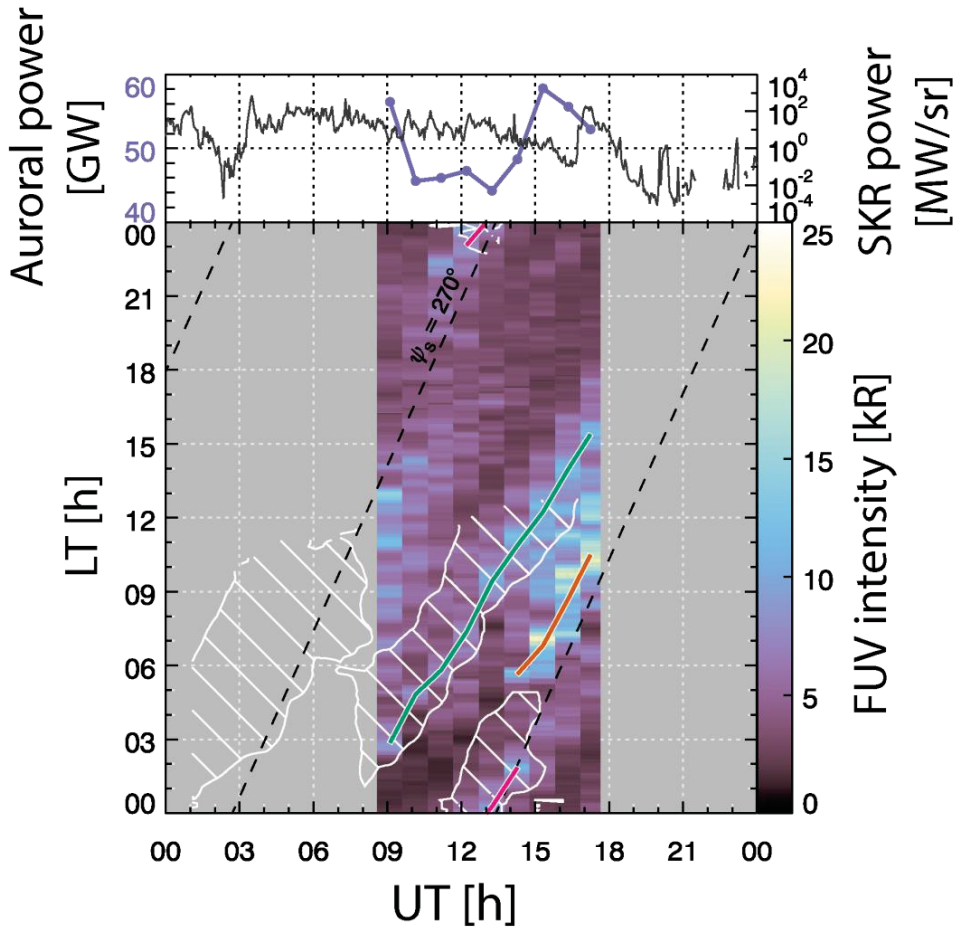

Figure 3. A keogram showing planet-projected FUV intensity plotted versus LT vertically and UT horizontally for 2014-099. Constructed from 9 UVIS pseudo-images, the sequence spans ~8.7 h, from 0837 to 1736 UT. Each UVIS exposure spans ~ 60 mins, except the last which spans ~44 mins. Intensity profiles (columns) show the maximum values between 0-30° colatitude throughout the local time range. The green, magenta and orange lines show the centroid motion of the three clearest auroral patches tracked using an intensity threshold on the polar-projected images. White contour-shaded areas outline regions of enhanced ENA flux in the magnetosphere identified in Figure 4. Diagonal black lines indicate where the rotating region of primary upward field-aligned PPO current is expected to modulate the auroral emission in the southern hemisphere (Ψ_S = 270°). The top panel shows the total emitted UV auroral power within 0-30° colatitude during each exposure, which is derived from non-projected UVIS imagery, and the total southern (left-hand polarised) SKR power (100-400 kHz).

3.2 ENA imagery

The INCA camera observed ENAs throughout most of day 2014-099 (up to ~1935 UT), from spacecraft distances of ~18-22 R_S. Cassini traversed a local time range of ~1430 -1830 LT and southern latitudes of ~31-41° during the observation window, providing the INCA a near-complete view of the morning-side magnetosphere. This is where the majority of transient injection signatures are observed in the ENA emission [e.g. *Mitchell et al.*, 2005; 2009; 2015]. An inclined orbit perspective is useful for quantifying azimuthal variation in the ENA flux (conversely, low-latitude ENA imagery provides a cross section of the radial flux distribution rather than the azimuthal). Making the assumption that the ENA emission originates from a thin emitting disc in the equatorial

564 plane (where most of the neutral density is confined [e.g. *Jurac & Richardson*, 2005], the INCA
565 images may be projected into the XY plane, resulting in a pseudo-map of the global ENA flux
566 distribution. Note that such projection involves converting a line-of-sight integral measurement
567 onto a two-dimensional plane, and the effective projection accuracy reduces with distance from the
568 spacecraft, particularly on low inclination orbits. For reference the projected INCA images from day
569 2014-099 are provided in the Supporting Information S1.
570
571 Keogram analysis is required to quantify the azimuthal speed of rotating ENA enhancements
572 captured within the grid-projected INCA images. Figure 4 shows local time profiles of the median
573 ENA flux intensity within 20.7 R_S of the planet, with each pixel column corresponding to a projected
574 ENA image (see S1). Column width equals the INCA integration time for each image. Plotted in the
575 same UT-LT frame as the auroral keogram in Figure 3, diagonal features with positive gradient
576 indicate an ENA flux enhancement rotating in the planetary direction. To guide the eye, white
577 contour lines are based on a smoothed image of the collective profiles ($1\times$ 19-pixel box car filter) at
578 an arbitrary level of 1.0 differential intensity counts per cm^2-sr-s-keV. Three main rotating features
579 are evident in the keogram. Signatures labelled E1 and E3 in Figure 4 are likely part of the same
580 rotating ENA feature that moved out of the INCA FOV at pre-noon, re-appearing ~ 6 h later at local
581 midnight with reduced intensity. Signature E3 dissipates by ~ 09 LT and does not make another
582 rotation around the planet. A second rotating ENA signature, labelled E2, formed in the morning
583 sector at ~07-08 UT, around 8 h after the appearance of E1 at similar local times. INCA only tracked
584 E2 until ~16 UT when it exited the field of view at local noon.
585
586 Lines of best fit to the maximum ENA flux intensity in each median profile are plotted for features
587 E1 and E2 in Figure 4 (black crosses and dashed lines), indicating sub-corotational azimuthal speeds
588 of ~0.68 and 0.70 Ω respectively. These estimates are typical of rotating ENA enhancements speeds
589 based on the statistical INCA survey of *Carbary* [2014], which used a similar keogram tracking
590 method.
591

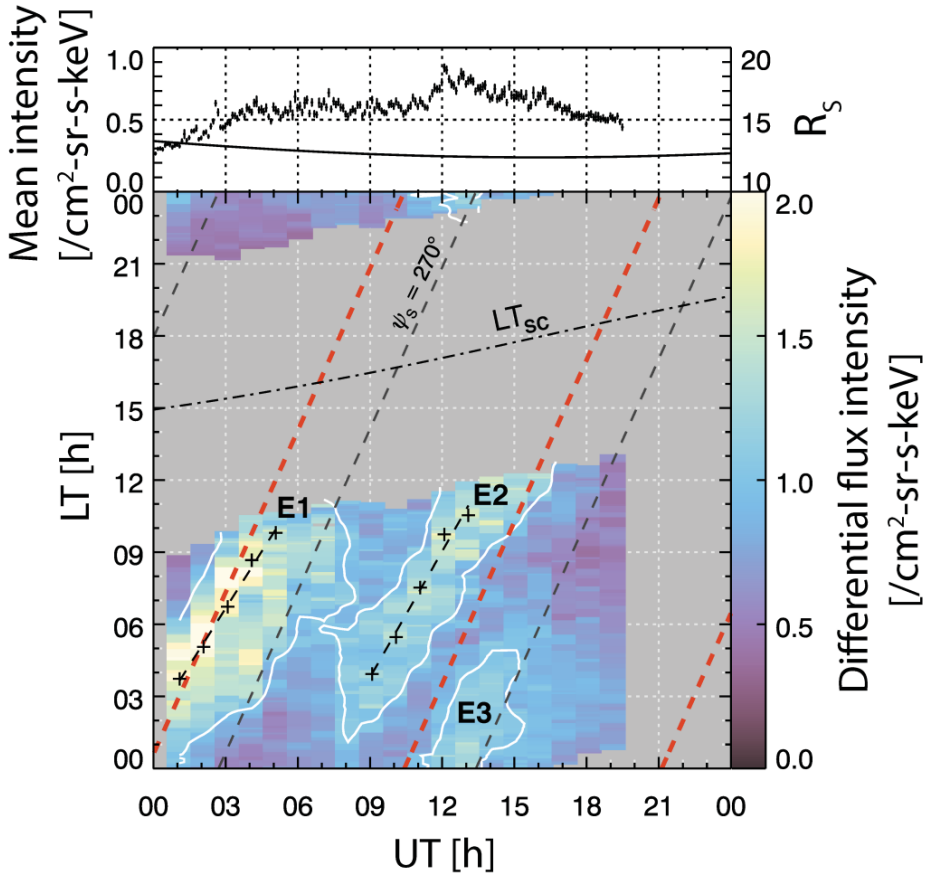

Figure 4. A keogram showing projected ENA flux distributed in UT versus LT throughout day 2014-099. Each flux profile (column) is built up of the median values of the magnetospheric equatorial projection between the planet and the assumed magnetopause mapping distance (20.7 R_S) across the local time range. Grey shading indicates missing data (local times outside the INCA FOV or lack of UT coverage). White contour lines, based on a smoothed image (1 × 19-pixel box car filter) at an arbitrary level of 1.0 differential intensity counts per cm²-sr-s-keV, outline the rotating ENA enhancements. Black crosses show maxima in selected median-based ENA flux profiles, with dashed lines of best fit indicating azimuthal speeds of ~ 68-70 % PPO corotation. The dot-dashed black line shows Cassini's local time position, LT_{SC}. Diagonal black lines indicate where the rotating region of primary upward field-aligned PPO current is expected to modulate the auroral emission in the southern hemisphere (Ψ_S = 270°). Red dashed lines show the expected location of magnetotail thinning by superposition of the north and south PPO perturbation fields in the equatorial plane. The top panel shows the global average differential flux intensity from the un-projected INCA images (black dots), together with spacecraft-planet distance (black line). Annotations E1, E2 and E3 mark the three rotating ENA signatures.

3.3 SKR Activity

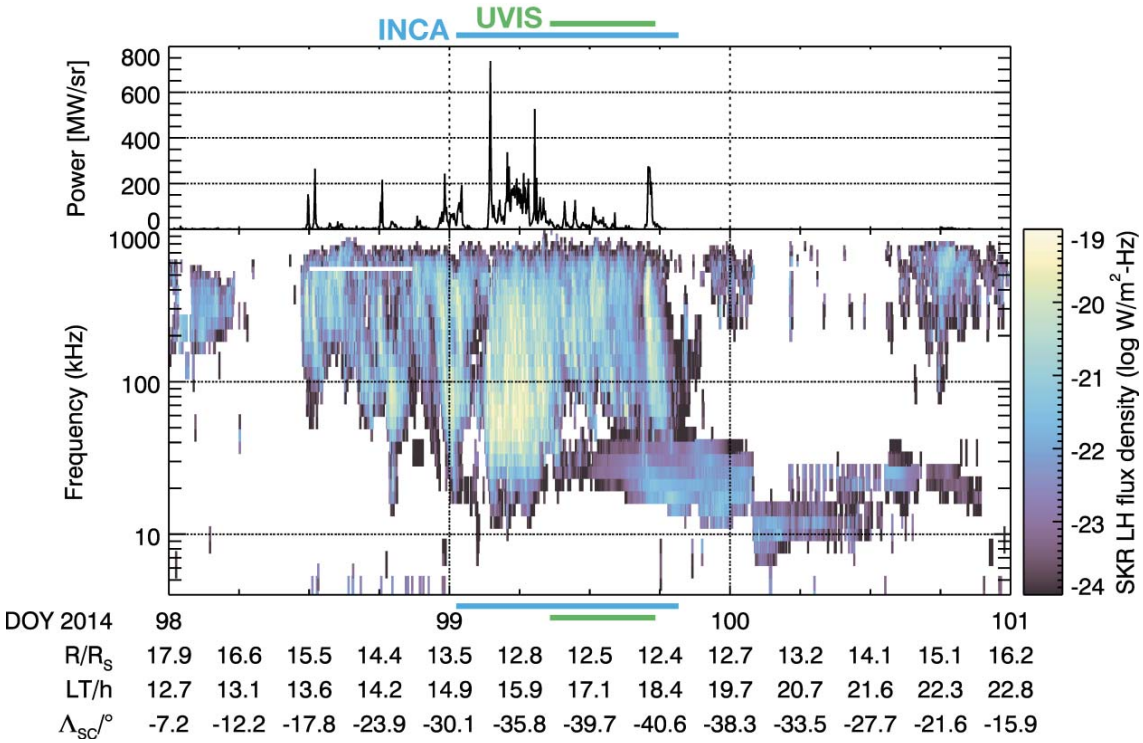

Figure 5. Cassini RPWS spectrogram, showing left-hand circular polarised (LHCP, Southern hemisphere) SKR emitted power (log-scaled color mapping) versus emission frequency and time, over days 98-100 in 2014. The data gap between 500-600 kHz on day 98 is present after filtering out radio interference artefacts [see *Lamy et al.*, 2008]. The top panel shows the total LHCP SKR emission power integrated between 10-1000 kHz. Blue and green lines above and below the plot indicate the time extents of the imaging windows provided by the INCA and UVIS respectively. Additional x-axis annotations show Cassini's planetary distance (R), local time (LT) and sub-spacecraft latitude (Λ_{SC}).

Figure 5 shows an electric field spectrogram from the Cassini RPWS instrument (bottom panel), showing the southern hemisphere (LH-polarized) SKR emission power versus frequency over days 98-100 of 2014. The top panel shows the total southern SKR emission power integrated between 10-1000 kHz, a frequency band that includes both the main SKR emission between 100-400 kHz, and the narrowband SKR emission (n-SKR) between 10-40 kHz. The SKR emission was clearly active from halfway through day 98 and into the end of the next day, 99. Multiple LFE signatures are visible from ~18 UT on day 98, with emission power and low frequency extension being greatest between ~03-09 UT on day 99. The total emission power also reflects this, having multiple peaks over 200 $MWsr^{-1}$ throughout these two days. The two largest power peaks occurred at ~04 UT (over 700 $MWsr^{-1}$) and ~07 UT (> 500 $MWsr^{-1}$) on day 99, within the INCA imaging window reported here (see blue line in Figure 5). Only a single power peak of > 200 $MWsr^{-1}$ falls within the UVIS imaging window (green line in Figure 5) at ~17 UT. The SKR response in Figure 5 lacks any clear sign of the characteristic rotational periodicity usually observed in the emission [e.g. *Lamy et al.*, 2008], but the measurement has a complex directional dependence, and both injection activity and solar wind compressions have been observed to interrupt this periodicity [e.g. *Badman et al.*, 2008, *Reed et al.*, 2018].

An extended period of narrowband SKR emission between 10-40 kHz follows the main period of LFE activity, beginning at ~1200 on day 99 and persisting until ~0200 the next day. This emission is

typically only observed when Cassini is in high-inclination orbits [*Lamy et al.*, 2008]. Although the exact source of the narrowband signature is unknown, presence of the emission has been associated with changes in the magnetospheric plasma density in the inner magnetosphere [*Louarn et al.*, 2007], possibly the edges of the plasma torus at L~ 4-7 [Ye et al., 2009]. The onset of the narrowband emission has also been observed to coincide with the presence of ENA enhancements rotating through the dusk-midnight sector imaged by INCA [*Wang et al.*, 2010].

4 Discussion

We now discuss the conjugacy of the rotating features observed in the auroral and ENA imagery, and the possible nature of the current system connecting them. We observe multiple signatures of plasma injection activity and, in each case, we consider possible rotational modulation in the frame of the PPO current systems (see Section 2.5).

4.1 Multiple injection signatures

The INCA imagery during day 2014-099 reveals the evolution of two rotating ENA flux enhancements that move through the morning sector, separated by a time of ~8 h UT. The first ENA patch, referred to in Section 2 and Figure 4 as E1, is present from the beginning of the observation window (0035-0135 UT), spanning most of the midnight-dawn sector. Based on previous surveys of recurrent ENA patches [e.g. *Mitchell et al.*, 2009, *Carbary et al.*, 2014], E1 is likely a signature of large-scale plasma injection following reconnection in the magnetotail, forming some hours before the INCA sequence presented here. An SKR southern power peak of > 200 MW sr^{-1} was detected at ~2330 UT on the previous day (2014-098), when the expected tail thinning PPO longitude sector was also approaching midnight LT (Ψ_S ~ 340°).

The largest SKR peak of ~ 700 MW sr^{-1} occurred at ~04 UT when E1 was moving through dawn, together with the region of maximum upward current expected from the rotating southern PPO current system. The SKR remained enhanced with peaks of ~200-350 MW sr^{-1} between ~05-07 UT as E1 moved into the dayside and intensified. The ENA intensity of the patch was at least twice that of the surrounding background levels, peaking between radial distances of ~15-25 R_S (given the resolution limits of the projected INCA pixels). We observe E1's rotation around the morning flank at a sub-corotational rate of ~0.68 Ω, before exiting the field of view pre-noon at ~07-08 UT. This behaviour is again consistent with an ENA signature of large-scale hot plasma injection following tail reconnection [e.g. *Mitchell et al.*, 2009, *Carbary & Mitchell*, 2014]. Coincident UVIS imagery was not available until ~0837 UT, so it was not possible to test for a matching auroral signature. However, the enhancement near noon present in the first UVIS image at ~0837 UT could be related to the passing of the ENA patch (see Figure 3).

It is likely that ENA feature E3, imaged in the midnight sector around 13-14 h later, is the remnant of the same injection signature E1, considering the earlier azimuthal speed estimate of ~0.68 Ω. By this time the injected ion population is likely to have been energy dispersed and spread in longitude, but ENA signatures commonly persist for longer than a planetary rotation [e.g. *Krimigis et al.*, 2005, *Paranicas et al.*, 2005, *Mitchell et al.*, 2009; 2015]. Although signature E3 dissipates before reaching dawn again, we do see an auroral counterpart at 00 LT, U2, at the same time as the ENA patch E3 is observed (~13-15 UT). The UVIS image sequence and patch tracking analysis indicates that U2 had moved from the dusk sector through midnight (Figures 1d-1f), where it brightened. Interestingly this intensity increase was coincident with the expected region of upward field-aligned current associated with the southern PPO current system (clearest in Figure 3). In this case, the re-brightening of the 'old' injection signature in the aurora at midnight may have resulted from direct

enhancement by the rotating PPO current. Auroral patch U2 maintained an azimuthal velocity of ~0.6 Ω, with centroid colatitudes of ~18° (i.e. equatorward of the morning sector signatures U1 & U3, which appear at ~15° colatitude). This is consistent with an older injected source region having moved inwards through the magnetosphere.

A second dawn-side injection signature was captured simultaneously in the ENA and auroral imagery over ~ 9 h, identified as E2 and U1 respectively. We first observe the injection signature in the midnight-morning sector at ~03 LT (~09 UT) in the aurora and slightly earlier in the ENA flux as a region several hours wide (~ 07-08 UT). A coincident peak in the global SKR power of over 500 MW sr^{-1} was also observed at ~07 UT, shortly before UVIS started imaging, suggesting that the peak auroral response occurred around this time in the midnight-early morning sector as the ENA flux intensified. At this time, the PPO current systems were aligned such that the region of expected magnetotail thinning was moving through the dusk region, possibly promoting reconnection in the tail [Bradley et al., 2018]. A significant bend-back of the field between the ionosphere and magnetosphere would therefore be required to link the appearance of the ENA and auroral signatures at ~03 LT with the thinned current sheet at ~18 LT. However, we note that the survey of *Bradley et al.* [2018] indicates that reconnection signatures in the tail do not necessarily coincide with times / locations when the current sheet is thinnest – but at some point approaching this, depending on how close to instability the tail is.

The local time position of signatures E2 and U1 remained similar during the following ~ 9 h UT, i.e. the centroid of the auroral signature appears to have tracked the ENA cloud in the magnetosphere until at least ~ 15 LT. We note that the LT extent or spread of signature E2 in the ENA keogram was consistently ~3-4 h, based on median profiles of all ENA flux recorded out to ~ 20 R_S. The LT spread of the auroral signature U1 was initially less than an hour, which then increased to several hours as the signature moved through the dayside (see Figure 2a).

Mitchell et al. [2009] argue that the presence of a rotating plasma asymmetry should set up a series of large-scale pressure-gradient driven field-aligned currents at its leading and trailing edges, much like a partial ring current at Earth [e.g. *Brandt et al.*, 2010]. Given the sense of magnetic gradient-curvature drifts of trapped particles in Saturn's magnetosphere, energetic electrons are expected to lag ions in the corotation frame, such that an injected plasma parcel may exhibit energy-dependent dispersive spread with time. *Nichols et al.* [2014] tracked the azimuthal speed of a rotating dayside auroral enhancement imaged with the HST following a storm event, which may then have mapped to the trailing edge of a particularly intense rotating ENA cloud imaged by INCA some hours later at dusk, assuming it maintained similar azimuthal speed. These authors proposed that the trailing edge of the ENA cloud may be close to the source of energetic electrons driving the trailing auroral signature via closure of upward FAC.

Lamy et al. [2013], reporting a similar rotating injection signature in coincident auroral and ENA imagery, did not observe a 'trailing edge' mapping between magnetosphere and ionosphere, but rather a broad longitude sector in the ENA emission that tracked the rotating auroral signature, as we see here. This may indicate an extended region of filamentary FACs that are unresolved in the auroral imagery, but which may be triggered by the larger-scale plasma pressure gradients at some point following the injection.

We must also consider the ENA energy ranges captured by the INCA and the relationship of this ion-based proxy to the electrons driving the auroral emissions. As mentioned above, the 1:1 LT mapping that we observe in some rotating auroral and ENA patches is a function of the relative particle energies producing the respective signatures, in this case the 24-55 keV injected population and auroral source electrons of typically 100s eV [e.g. *Bunce et al.*, 2008]. Sometime after an

injection event, the velocity of the plasma ω_{TOT} will be determined by the bulk convection flow, ω_{CON}, together with a gradient-curvature drift proportional to the particle energies, ω_{GC}:

$$\omega_{TOT} = \omega_{CON} \pm \omega_{GC} \qquad (2)$$

We can estimate the expected gradient-curvature drift rates of injected ions and electrons in a dipole field following *Mauk et al.* [2005] or *Thomsen & Van Allen* [1980]:

$$\omega_{GC} = 3.94\times10^{-5}\frac{q_0}{q}E_{MeV}\frac{\left(\frac{E_{MeV}}{2}+m_0c^2\right)}{(E_{MeV}+m_0c^2)}LH(\alpha) \qquad (3)$$

Here E_{MeV} is the particle energy in MeV, m_0 is the particle rest mass, q_0 is the unit charge, q is charge, c is light speed, and α is the equatorial pitch angle. L, the magnetic L shell number, is estimated here with the dipole $R/\cos^2(\lambda)$, where R is radial distance in R_S and λ is magnetic latitude. $H(\alpha)$ is a pitch angle dependence factor, estimated after *Hamlin et al.* [1961] as $H \cong 0.7 + 0.3\sin\alpha$. In the equatorial plane and assuming pitch angles of 90°, H ≅ 1 and L = R assuming a dipolar field. The ENA imagery presented in this study was captured in the energy range 24-55 keV, yielding drift speeds of between $\omega_{GC} \approx \pm$ 1.5-3° per hour at 15 R_S, with electrons and ions (of these energies) drifting behind and ahead of the bulk plasma convection respectively.

For particles with energy < 1 keV, however, gradient-curvature drift is negligible, and they drift at the bulk flow convection speed. In relating the apparent ENA and auroral signatures, we may say that the effective drift between 24-55 keV injected ions and auroral source electrons (100s of eV) is between ~1.5-3° per hour. For example, after 10 hours from an injection event, we might expect a separation of 15-30° azimuth (or 1-2 h LT) between the two signatures. Given the exposure times (~ 1 h) and resolution constraints of the images, we cannot resolve this spread with less than ~ 10 h UT continuous observation. This is consistent with the 'oldest' auroral (U_2 in Figure 1d) and ENA (E_3 in Figure 4) signature pair observed here; there isn't a systematic LT offset between the two.

4.2 An auroral injection signature with no ENA counterpart

The end of the UVIS sequence shows auroral activity in the absence of any obvious ENA flux increase. We tracked a clear rotating auroral patch, U_3 (orange trace in Figures, 1, 2 & 4), which developed in the same way as the preceding patch U_1 ~ 4 h earlier; broadening and moving equatorward while sub-corotating at ~0.73 Ω, likely an injection signature. The INCA field-of-view maintained almost complete coverage of the morning sector out to ~ 20 R_S, so it is curious that there is no clear ENA counterpart to auroral patch U_3. This is clearest when comparing the ENA and auroral keograms in Figures 4 & 6. Auroral patches U_1 and U_3 both tracked at similar colatitudes in the ionosphere (see Figure 2b), so we expect the source regions to have mapped to regions of similar neutral density. From equation (1), a reduction in ENA flux should then be caused by either a decrease in ion flux or energy. The bulk plasma flow in the morning sector would have been mostly perpendicular to the INCA's pointing direction from dusk in both cases, such that the Compton-Getting effect on detected ENAs would be minimal (additionally there was no clear rotating signature in the 55-90 keV H INCA band, which we do not report here). A difference of several hours LT traversal in spacecraft position may have shifted the viewing geometry enough such that, by the time auroral patch U_3 was developing, the isotropic distribution of ENAs was either too weak to detect from this pre-noon location, or was outside INCA's FOV.

There is no clear rotating signature in the 55-90 keV H INCA band, so perhaps lower energy ions were producing lower energy ENAs (or indeed any at all), not detected by the INCA. Figures 1 and 3 show that patch U3 did track more closely to the expected maximum upward field-aligned current region from the southern PPO system (several hours of LT ahead), compared to patch U1 (almost 12 hours ahead i.e. in the expected downward current region), so it is feasible that U3 was modulated more directly by PPO current rather than a transient connection with an injection source region in the magnetosphere. In any case, an important conclusion to draw from these data is that rotating ENA and UV injection signatures are not always proxies for each other.

4.3 Do we detect a plasmapause-like boundary?

The tracked equatorward centroid motion of patch U1 implies a radial speed reduction of the auroral source region by approximately an order of magnitude at some boundary between ~14-20 R_S. Based on compressed/expanded magnetospheric mapping profiles (see Section 2.4), the inward radial speed reduced from 44-54 km s^{-1} to 7-9 km s^{-1}. The patch's azimuthal motion remained constant as it traversed dayside local times, showing no signs of the previously reported 'stagnation' point around noon [*Radioti et al.*, 2017]. Interestingly this 'braking' in radial speed was coincident with the patch brightening (Figure 2c).

How do we explain this slowing down of the auroral source region with brightening of the UV intensity? The radial braking may be associated with the dipolar field boundary [*Arridge et al.*, 2008] or plasmapause-like transition region reported by *Thomsen et al.* [2015], indicating a point at which entropy or equilibrium is reached with the ambient plasma [e.g. *Wolf et al.*, 2009]. *Thomsen et al.* [2015] reported an abrupt plasma pressure gradient at distance L ~ 8.6 during a fast, inclined Cassini orbit from the northern lobe into the night-side closed field region, which (as those authors indicate) would have likely mapped to at least 15 R_S in the magnetotail. The reduced speed estimate above is also consistent with inward interchange flows inferred from particle measurements towards the inner magnetosphere [e.g. *Paranicas et al.*, 2016].

Plasma pressure gradients in the middle-inner magnetosphere are expected following tail injection activity, when the radial interchange instability sets up filamentary plasma flow channels [e.g. *Thomsen et al.*, 2013, *Paranicas et al.*, 2016, *Mauk et al.*, 2005]. It is thought that as the injected hot plasma from large-scale events flows inwards and rotates under background convection, it gradually coats or envelops the cold, inner magnetosphere plasma, promoting the further development of interchange instabilities [e.g. *Thomsen et al.*, 2015, *Azari et al.*, 2018]. Aside from the observed injection activity, this picture is supported here by the detection of prolonged narrowband SKR emission following the injection activity, produced preferentially in regions of pronounced plasma pressure gradient [*Louarn et al.*, 2007, *Ye et al.*, 2009]. An equatorial bifurcation of the main auroral emission post-noon (see Figures 1h-i) appears similar to that reported by *Radioti et al.* [2013] as a signature of interchange activity driving wave-particle scattering.

In terms of the auroral intensity increase, we may consider the effect of the source region moving gradually inwards through the magnetosphere, convecting into regions of higher field strength and shorter field lines. Convection flow channels move closer to the planet as the solar wind pressure deforms the dayside magnetopause (an effect which also augments the ENA intensity as ions move into regions of higher neutral density). Firstly, the increased loss cone would drive up the energy flux of precipitating particles into the atmosphere. If magnetic moment is conserved, adiabatic heating will also increase the perpendicular energy of trapped particles – possibly further scattering particles into the loss cone through wave-particle interactions [e.g. *Mauk et al.*, 2005, *Paranicas et*

844 *al.*, 2016]. At Saturn, plasma energy may be augmented by factors of ~2-3 through adiabatic
845 heating as it moves towards the dayside [e.g. *Badman & Cowley*, 2007].
846
847 The approximate bounce period of a 24 keV ion (electron) between 10-20 R_S is ~ 50 (1) min
848 (following the formulation in *Baumjohann & Treumann*, [2012]), which is shorter than the ~ 6 h it
849 takes auroral patch U1 to move from dawn to dusk. Therefore, conservation of the longitudinal
850 invariant (resulting from a change in particle path length) may also have increased the parallel
851 particle energy of the source population as it moved radially inwards. We note that the auroral
852 patch brightened as it moved into the dayside where ionospheric conductivities are expected to
853 increase under sunlight [e.g. *Galand et al.,* 2011], but this effect is expected to be minimal here as
854 the southern hemisphere was in winter.
855
856 The wider dayside aurora brightened in the final three frames of the UVIS sequence (~15-19 UT),
857 resulting in the emitted power increase up to 50-60 GW as shown in the top panel of Figure 3. There
858 was also a clear increase in the dayside infrared auroral emissions measured by Cassini's Visible and
859 Infrared Mapping Spectrometer (VIMS) at the same time (not reported here), indicating a period of
860 increased precipitating energy flux along auroral field lines. An SKR peak of > 200 MW sr^{-1} was
861 measured at ~17 UT (when patch U3 was moving through mid-morning LTs), but the total southern
862 radio emission power had generally started to weaken by this time (see Figure 5). This broad
863 dayside intensification may indicate a compression of the dayside plasma flow channels toward the
864 end of the UVIS sequence, further enhancing the effects discussed above. Cassini was located well
865 inside the magnetopause at ~12.5 R_S radial distance and ~40° latitude, so we are unable to say if
866 there was also an external solar wind compression of the magnetopause at that time.
867
868

869 # 5 Summary
870
871 Here we highlight a case study using partially coincident auroral and ENA images captured during a
872 southern high latitude Cassini orbit on 9 April 2014 (including ~8 h of overlap), in which three
873 injection signatures are observed at various stages of development. SKR emissions also indicate
874 significant injection activity throughout the day. We attempted to track the location and extents of
875 these injection signatures in the auroral and ENA imagery to test if they are counterpart. We have
876 quantified (to the extent that we can) the motion of the hot plasma distribution using global ENA
877 emissions, mainly in the azimuthal frame due to the coarse nature of the native INCA pixel grid
878 projection in the radial direction. The motion of rotating FUV auroral patches is tracked in both local
879 time and latitude, and a local-time symmetric mapping model was used to estimate the radial
880 distance and inflow speeds of a hypothetical source region in the magnetosphere for compressed
881 and expanded plasma pressure states.
882
883 We find an approximate 1:1 local time mapping within the limitations of respective azimuthal image
884 resolutions, maintained throughout the lifetime of two injection events. This show that large-scale
885 ENA injections can evidently map to auroral latitudes, not necessarily equatorward of them, as
886 indicated by the *Carbary et al.* [2008] statistical study. In a third case, however, a clear auroral
887 injection signature has no obvious match in the ENA imagery. An important conclusion to draw
888 from these data is that rotating ENA and UV injection signatures are not always proxies for each
889 other, and their relationship is likely to be a function of plasma source energy and viewing angle
890 geometry. We also report possible rotational modulation of an older auroral injection signature as it
891 passed through the midnight sector and brightened. This modulation may be related to upward
892 field-aligned current associated with the planetary-period perturbation field [e.g. *Bader et al.*,
893 2018], or recurrent energization of the source region in the tail [e.g. *Mitchell et al.*, 2009].

We also observe 'braking' of the inward motion of a plasma injection, manifesting here as a marked slowing down of the equatorward motion of an auroral signature (mapped radial speed estimates in the magnetosphere slow from ~44-54 km s^{-1} to ~7-9 km s^{-1}). This may be due to the presence of a plasmapause-like boundary. Further evidence of radial flow boundaries extrapolated from remotely-sensed auroral imagery might be useful but relies on improved magnetic mapping models (for example, *Sorba et al.* [2019] have recently computed local-time-dependent ionosphere-magnetodisc mapping profiles at Saturn).

6 Acknowledgements

UVIS, INCA and RPWS data are available from the NASA Planetary Data System (https://pds.jpl.nasa.gov). SKR power and spectrogram data were retrieved through the AMDA science analysis system provided by the Centre de Données de la Physique des Plasmas (CDPP) supported by CNRS, CNES, Observatoire de Paris and Université Paul Sabatier, Toulouse. All PPO phase data (2004–2017) are available in the University of Leicester Research Archive (http://hdl.handle.net/ 2381/42436). We thank Nick Achilleos and Arianna Sorba at UCL for their provision of ionosphere-magnetosphere field mapping profiles, which have since been computed for various local time sectors, and are available in the Supporting Information of *Sorba et al.* [2019].

JK, SVB, and CSA were supported by STFC grant ST/M001059/1. JK was also supported by a DST-NRF Fellowship for Early Career Researchers in the United Kingdom (UID: 110706), and thanks Dr Zama Katamzi-Joseph and Prof. Mike Kosch at the South African National Space Agency for hosting him on a research visit. SVB was also supported by an STFC Ernest Rutherford Fellowship ST/M005534/1, and CSA also by a Royal Society Research Fellowship. CP was supported by NASA grant NNX16AI46G. DGM was supported by NASA grant NNN06AA01C. AB was funded by a Lancaster University FST studentship. GP and SWHC were supported by STFC grant ST/N000749/1. CJM was supported by STFC grant ST/R000816/1. NA was supported by the UCL STFC Solar System Consolidated Grant ST/S000240/1. RLG was supported by an STFC studentship.

7 References

Achilleos, N., Arridge, C. S., Bertucci, C., Jackman, C. M., Dougherty, M. K., Khurana, K. K., and Russell, C. T. (2008). Large-scale dynamics of Saturn's magnetopause: Observations by Cassini. *J. Geophys. Res.*, 113, A11209, doi:10.1029/2008JA013265.

Achilleos, N., Guio, P., Arridge, C. S., Sergis, N., Wilson, R. J., Thomsen, M. F., and Coates, A. J. (2010). Influence of hot plasma pressure on the global structure of Saturn's magnetodisk. *Geophys. Res. Lett.*, 37, L20201, doi:10.1029/2010GL045159.

Arridge, C. S., Khurana, K. K., Russell, C. T., Southwood, D. J., Achilleos, N., Dougherty, M. K., Coates, A. J., and Leinweber, H. K. (2008). Warping of Saturn's magnetospheric and magnetotail current sheets. *J. Geophys. Res.*, 113, A08217, doi:10.1029/2007JA012963.

Arridge, C. S., Eastwood, J. P., Jackman, C. M., Poh, G. –K., Salvin, J. A., Thomsen, M. F., et al. (2016). Cassini in situ observations of long-duration magnetic reconnection in Saturn's magnetotail. *Nature Physics*, 12, 268-271, https://doi.org/10.1038/nphys3565.

Azari, A. R., Liemohn, M. W., Jia, X., Thomsen, M. F., Mitchell, D. G., Sergis, N., et al. (2018). Interchange injections at Saturn: Statistical survey of energetic H+ sudden flux intensifications. *Journal of Geophysical Research: Space Physics*, 123, 4692–4711. https://doi.org/10.1029/2018JA025391.

Bader, A., Badman, S. V., Kinrade, J., Cowley, S. W. H., Provan, G., & Pryor, W. R. (2018). Statistical planetary period oscillation signatures in Saturn's UV auroral intensity. *Journal of Geophysical Research: Space Physics*, 123, 8459– 8472. https://doi.org/10.1029/2018JA025855

Bader, A., Badman, S. V., Kinrade, J., Cowley, S. W. H., Provan, G., & Pryor, W. (2019a). Modulations of Saturn's UV auroral oval location by planetary period oscillations. *Journal of Geophysical Research: Space Physics*, 124, 952– 970. https://doi.org/10.1029/2018JA026117.

Bader, A., Badman, S. V., Cowley, S. W. H., Yao, Z. H., Ray, L. C., Kinrade, J., et al. (2019b). The dynamics of Saturn's main aurorae. *Geophysical Research Letters*, 46. https://doi.org/10.1029/2019GL084620.

Badman, S. V., Cowley, S. W. H., Gérard, J.-C., and Grodent, D. (2006). A statistical analysis of the location and width of Saturn's southern auroras. *Annales Geophysicae*, European Geosciences Union, 24 (12), 3533-3545, https://doi.org/10.5194/angeo-24-3533-2006.

Badman, S. V. and Cowley, S. W. H. (2007). Significance of Dungey-cycle flows in Jupiter's and Saturn's magnetospheres, and their identification on closed equatorial field lines. *Ann. Geophys.*, 25, 941–951, https://doi.org/10.5194/angeo-25-941-2007.

Badman, S. V., Cowley, S. W. H., Lamy, L., Cecconi, B., & Zarka, P. (2008). Relationship between solar wind corotating interaction regions and the phasing and intensity of Saturn kilometric radiation bursts. *Annales Geophysicae*, 26(12), 3641-3651. https://doi.org/10.5194/angeo-26-3641-2008.

Bagenal, F., and Delamere, P. A. (2011). Flow of mass and energy in the magnetospheres of Jupiter and Saturn. *J. Geophys. Res.*, 116, A05209, doi:10.1029/2010JA016294.

Baumjohann, W. and Treumann, R. A. (2012), Basic Space Plasma Physics: Revised Edition, Imperial College Press (London), ISBN:10-1-84816-895-0.

Bradley, T. J., Cowley, S. W. H., Bunce, E. J., Smith, A. W., Jackman, C. M., & Provan, G. (2018). Planetary period modulation of reconnection bursts in Saturn's magnetotail. *Journal of Geophysical Research: Space Physics*, 123, 9476– 9507. https://doi.org/10.1029/2018JA025932.

Brandt, P. C., Mitchell, D. G., Roelof, E. C., Krimigis, S., Paranicas, C., Mauk, B., et al. (2005), ENA imaging: Seeing the invisible. *Johns Hopkins APL Technical Digest (Applied Physics Laboratory)*, 26 (2), 143-154.

Brandt, P. C., Hsieh, S. Y., DeMajistre, R., and Mitchell, D. G. (2018). ENA Imaging of Planetary Ring Currents. In *Electric Currents in Geospace and Beyond*, Part II: Ring Currents, Chapter 6, American Geophysical Union, July 2018, ISBN: 978-1-119-32449-2.

992 Bunce, E. J., Cowley, S. W. H., Wright, D. M., Coates, A. J., Dougherty, M. K., Krupp, N., Kurth, W.
993 S., and Rymer, A. M. (2005). In situ observations of a solar wind compression-induced hot plasma
994 injection in Saturn's tail. *Geophys. Res. Lett.*, 32, L20S04, doi:10.1029/2005GL022888.
995
996 Burch, J. L., Goldstein, J., Hill, T. W., Young, D. T., Crary, F. J., Coates, A. J., André, N., Kurth, W. S.,
997 and Sittler, E. C. (2005). Properties of local plasma injections in Saturn's magnetosphere. *Geophys.*
998 *Res. Lett.*, 32, L14S02, doi:10.1029/2005GL022611.
999
1000 Burger, M. H., Sittler, E. C., Johnson, R. E., Smith, H. T., Tucker, O. J., and Shematovich, V. I. (2007).
1001 Understanding the escape of water from Enceladus. *J. Geophys. Res.*, 112, A06219,
1002 doi:10.1029/2006JA012086.
1003
1004 Carbary, J. F., Mitchell, D. G., Brandt, P., Roelof, E. C., and Krimigis, S. M. (2008). Statistical
1005 morphology of ENA emissions at Saturn. *J. Geophys. Res.*,113, A05210, doi:10.1029/2007JA012873.
1006
1007 Carbary, J. F., and Mitchell, D. G. (2013). Periodicities in Saturn's magnetosphere. *Rev. Geophys.*, 51,
1008 1-30, doi:10.1002/rog.20006.
1009
1010 Carbary, J. F., and Mitchell, D. G. (2014). Keogram analysis of ENA images at Saturn. *J. Geophys.*
1011 *Res. Space Physics*, 119, 1771– 1780, doi:10.1002/2014JA019784.
1012
1013 Carbary, J., Hedman, M., Hill, T., Jia, X., Kurth, W., Lamy, L., & Provan, G. (2018). The Mysterious
1014 Periodicities of Saturn: Clues to the Rotation Rate of the Planet. In K. Baines, F. Flasar, N. Krupp, &
1015 T. Stallard (Eds.), *Saturn in the 21st Century* (Cambridge Planetary Science, pp. 97-125). Cambridge:
1016 Cambridge University Press. doi:10.1017/97813162272220.005.
1017
1018 Chen, Y., and Hill, T. W. (2008). Statistical analysis of injection/dispersion events in Saturn's inner
1019 magnetosphere. *J. Geophys. Res.*, 113, A07215, doi:10.1029/2008JA013166.
1020
1021 Chen, Y., Hill, T. W., Rymer, A. M., and Wilson, R. J. (2010). Rate of radial transport of plasma in
1022 Saturn's inner magnetosphere. *J. Geophys. Res.*, 115, A10211, doi:10.1029/2010JA015412.
1023
1024 Cowley, S. W. H., Bunce, E. J., and O'Rourke, J. M. (2004). A simple quantitative model of plasma
1025 flows and currents in Saturn's polar ionosphere. *J. Geophys. Res.*, 109, A05212,
1026 doi:10.1029/2003JA010375.
1027
1028 Cowley, S. W. H., Badman, S. V., Bunce, E. J., Clarke, J. T., Gérard, J.-C., Grodent, D., Jackman, C.
1029 M., Milan, S. E., and Yeoman, T. K. (2005). Reconnection in a rotation-dominated magnetosphere
1030 and its relation to Saturn's auroral dynamics. *J. Geophys. Res.*, 110, A02201,
1031 doi:10.1029/2004JA010796.
1032
1033 Cowley, S. W. H., and Provan, G. (2016). Planetary period oscillations in Saturn's magnetosphere:
1034 Further comments on the relationship between post-equinox properties deduced from magnetic
1035 field and Saturn kilometric radiation measurements. *Icarus*, 272, 258-276,
1036 https://doi.org/10.1016/j.icarus.2016.02.051.
1037
1038 Cowley, S. W. H., Provan, G., Hunt, G. J., and Jackman, C. M. (2017). Planetary period modulations
1039 of Saturn's magnetotail current sheet: A simple illustrative mathematical model. *J. Geophys. Res.*
1040 *Space Physics*, 122, 258– 279, doi:10.1002/2016JA023367.
1041

Esposito, L.W., Barth, C.A., Colwell, J.E., et al. (2004), The Cassini Ultraviolet Imaging Spectrograph Investigation. *Space Science Reviews*, 115 (1-4), 299-361, https://doi.org/10.1007/s11214-004-1455-8.

Galand, M., Moore, L., Mueller-Wodarg, I., Mendillo, M., and Miller, S. (2011). Response of Saturn's auroral ionosphere to electron precipitation: Electron density, electron temperature, and electrical conductivity. *J. Geophys. Res.*, 116, A09306, doi:10.1029/2010JA016412.

Galopeau, P. H. M., and Lecacheux, A. (2000). Variations of Saturn's radio rotation period measured at kilometer wavelengths. *J. Geophys. Res.*, 105 (A6), 13089– 13101, doi:10.1029/1999JA005089.

Gérard, J.-C., Bonfond, B., Gustin, J., Grodent, D., Clarke, J. T., Bisikalo, D., and Shematovich, V. (2009). Altitude of Saturn's aurora and its implications for the characteristic energy of precipitated electrons. *Geophys. Res. Lett.*, 36, L02202, doi:10.1029/2008GL036554.

Guo, R. L., Yao, H., Wei, Y., Ray, L. C., Rae, I. J., Arridge, C. S., et al. (2018). Rotationally driven magnetic reconnection in Saturn's dayside. *Nature Astronomy*, 2, 640-645, https://doi.org/10.1038/s41550-018-0461-9.

Gurnett, D. A., Kurth, W. S., Kirchner, D. L., Hospodarsky, G. B., Averkamp, T. F., Zarka, P., et al. (2004). The Cassini Radio and Plasma Wave Investigation, *Space Science Reviews*, 114 (1-4), 395-463, https://doi.org/10.1007/s11214-004-1434-0.

Gurnett, D. A., Lecacheux, A., Kurth, W. S., Persoon, A. M., Groene, J. B., Lamy, L., Zarka, P., and Carbary, J. F. (2009). Discovery of a north-south asymmetry in Saturn's radio rotation period. *Geophys. Res. Lett.*, 36, L16102, doi:10.1029/2009GL039621.

Gustin, J., Grodent, D., Radioti, A., Pryor, W., Lamy, L., & Ajello, J. (2017). Statistical study of Saturn's auroral electron properties with Cassini/UVIS FUV spectral images. *Icarus*, 284, 264-283. https://doi.org/10.1016/j.icarus.2016.11.017.

Hamlin, D. A., Karplus, R., Vik, R. C., & Watson, K. M. (1961). Mirror and azimuthal drift frequencies for geomagnetically trapped particles. *Journal of Geophysical Research,* 66 (1), 1–4. https://doi.org/10.1029/JZ066i001p00001.

Hill, T. (1979). Inertial limit on corotation. *J. Geophys. Res.*, 84 (A11), 6554– 6558, doi:10.1029/JA084iA11p06554.

Hill, T. W., Rymer, A. M., Burch, J. L., Crary, F. J., Young, D. T., Thomsen, M. F., Delapp, D., André, N., Coates, A. J., and Lewis, G. R. (2005). Evidence for rotationally driven plasma transport in Saturn's magnetosphere. *Geophys. Res. Lett.*, 32, L14S10, doi:10.1029/2005GL022620.

Hill, T. W., et al. (2008). Plasmoids in Saturn's magnetotail. *J. Geophys. Res.*, 113, A01214, doi:10.1029/2007JA012626.

Hunt, G. J., Cowley, S. W. H., Provan, G., Bunce, E. J., Alexeev, I. I., Belenkaya, E. S., et al. (2015). Field-aligned currents in Saturn's southern nightside magnetosphere: Subcorotation and planetary period oscillation components. *J. Geophys. Res. Space Physics*, 119, 9847- 9899, doi:10.1002/2014JA020506.

Jackman, C. M., Lamy, L., Freeman, M. P., Zarka, P., Cecconi, B., Kurth, W. S., Cowley, S. W. H., and Dougherty, M. K. (2009). On the character and distribution of lower-frequency radio emissions at

1093 Saturn and their relationship to substorm-like events. *J. Geophys. Res.*, 114, A08211,
1094 doi:10.1029/2008JA013997.
1095
1096 Jackman, C. M., Slavin, J. A., and Cowley, S. W. H. (2011). Cassini observations of plasmoid structure
1097 and dynamics: Implications for the role of magnetic reconnection in magnetospheric circulation at
1098 Saturn. *J. Geophys. Res.*, 116, A10212, doi:10.1029/2011JA016682.
1099
1100 Jackman, C. M., Achilleos, N., Cowley, S. W. H., Bunce, E. J., Radioti, A. K., Grodent, D., et al. (2013).
1101 Auroral counterpart of magnetic field dipolarizations in Saturn's tail. *Planetary and Space Science*,
1102 82-82, 34-42, https://doi.org/10.1016/j.pss.2013.03.010.
1103
1104 Jackman, C. M., et al. (2014). Saturn's dynamic magnetotail: A comprehensive magnetic field and
1105 plasma survey of plasmoids and traveling compression regions and their role in global
1106 magnetospheric dynamics. *J. Geophys. Res. Space Physics*, 119, 5465– 5494,
1107 doi:10.1002/2013JA019388.
1108
1109 Jackman, C. M., Provan, G., and Cowley, S. W. H. (2016). Reconnection events in Saturn's
1110 magnetotail: Dependence of plasmoid occurrence on planetary period oscillation phase. *J. Geophys.*
1111 *Res. Space Physics*, 121, 2922– 2934, doi:10.1002/2015JA021985.
1112
1113 Jia, X., Hansen, K. C., Gombosi, T. I., Kivelson, M. G., Tóth, G., DeZeeuw, D. L., and Ridley, A. J.
1114 (2012). Magnetospheric configuration and dynamics of Saturn's magnetosphere: A global MHD
1115 simulation. *J. Geophys. Res.*, 117, A05225, doi:10.1029/2012JA017575.
1116
1117 Jurac, S., McGrath, M. A., Johnson, R. E., Richardson, J. D., Vasyliunas, V. M., and Eviatar, A. (2002).
1118 Saturn: Search for a missing water source. *Geophys. Res. Lett.*, 29 (24), 2172,
1119 doi:10.1029/2002GL015855.
1120
1121 Jurac, S., and Richardson, J. D. (2005), A self-consistent model of plasma and neutrals at Saturn:
1122 Neutral cloud morphology. *J. Geophys. Res.*, 110, A09220, doi:10.1029/2004JA010635.
1123
1124 Kane, M., Mitchell, D. G., Carbary, J. F., Krimigis, S. M., and Crary, F. J. (2008). Plasma convection in
1125 Saturn's outer magnetosphere determined from ions detected by the Cassini INCA experiment.
1126 *Geophys. Res. Lett.*, 35, L04102, doi:10.1029/2007GL032342.
1127
1128 Kellett, S., Arridge, C. S., Bunce, E. J., Coates, A. J., Cowley, S. W. H., Dougherty, M. K., Persoon, A.
1129 M., Sergis, N., and Wilson, R. J. (2011). Saturn's ring current: Local time dependence and temporal
1130 variability. *J. Geophys. Res.*, 116, A05220, doi:10.1029/2010JA016216.
1131
1132 Kennelly, T. J., Leisner, J. S., Hospodarsky, G. B., and Gurnett, D. A. (2013). Ordering of injection
1133 events within Saturnian SLS longitude and local time. *J. Geophys. Res. Space Physics*, 118, 832– 838,
1134 doi:10.1002/jgra.50152.
1135
1136 Kivelson, M. G., and Southwood, D. J. (2005). Dynamical consequences of two modes of centrifugal
1137 instability in Jupiter's outer magnetosphere. *J. Geophys. Res.*, 110, A12209,
1138 doi:10.1029/2005JA011176.
1139
1140 Kivelson, M. G., and Jia, X. (2014). *Modulation of young injection events at Saturn at the rotation*
1141 *period of perturbations in the winter hemisphere: a proposed mechanism*. Paper presented at AGU Fall
1142 Meeting 2014, San Francisco, USA.
1143

Krimigis, S.M., Mitchell, D.G., Hamilton, D.C., Livi, S., Dandouras, J., Jaskulek, S., et al. (2004). Magnetosphere Imaging Instrument (MIMI) on the Cassini Mission to Saturn/Titan. *Space Sci. Rev.*, 114: 233. https://doi.org/10.1007/s11214-004-1410-8

Krimigis, S. M., et al. (2005). Dynamics of Saturn's magnetosphere from MIMI during Cassini's orbital insertion. *Science*, 307 (5713), 1270-1273, doi:10.1126/science.1105978.

Lamy, L., Zarka, P., Cecconi, B., Prangé, R., Kurth, W. S., and Gurnett, D. A. (2008), Saturn kilometric radiation: Average and statistical properties, *J. Geophys. Res.*, 113, A07201, doi:10.1029/2007JA012900.

Lamy, L., Cecconi, B., Prangé, R., Zarka, P., Nichols, J. D., and Clarke, J. T. (2009), An auroral oval at the footprint of Saturn's kilometric radio sources, colocated with the UV aurorae, *J. Geophys. Res.*, 114, A10212, doi:10.1029/2009JA014401.

Lamy, L., Prangé, R., Pryor, W., Gustin, J., Badman, S. V., Melin, H., Stallard, T., Mitchell, D. G., and Brandt, P. C. (2013). Multispectral simultaneous diagnosis of Saturn's aurorae throughout a planetary rotation. *J. Geophys. Res. Space Physics*, 118, 4817– 4843, doi:10.1002/jgra.50404.

Louarn, P., et al. (2007). Observation of similar radio signatures at Saturn and Jupiter: Implications for the magnetospheric dynamics. *Geophys. Res. Lett.*, 34, L20113, doi:10.1029/2007GL030368.

Mauk, B. H., et al. (2005). Energetic particle injections in Saturn's magnetosphere. *Geophys. Res. Lett.*, 32, L14S05, doi:10.1029/2005GL022485.

McAndrews, H. J., Thomsen, M. F., Arridge, C. S., Jackman, C. M., Wilson, R. J., Henderson, M. G., et al. (2009). Plasma in Saturn's nightside magnetosphere and the implications for global circulation. *Planetary and Space Science*, 57 (14-15), 1714-1722, https://doi.org/10.1016/j.pss.2009.03.003.

Meredith, C. J., Alexeev, I. I., Badman, S. V., Belenkaya, E. S., Cowley, S. W. H., Dougherty, et al. (2014), Saturn's dayside ultraviolet auroras: Evidence for morphological dependence on the direction of the upstream interplanetary magnetic field. *J. Geophys. Res. Space Physics*, 119, 1994–2008, doi:10.1002/2013JA019598.

Mitchell, D. G., et al. (2005). Energetic ion acceleration in Saturn's magnetotail: Substorms at Saturn? *Geophys. Res. Lett.*, 32, L20S01, doi:10.1029/2005GL022647.

Mitchell, D. G., Krimigis, S. M., Paranicas, C., Brandt, P.C., Carbary, J. F., Roelof, E.C., et al. (2009). Recurrent energization of plasma in the midnight-to-dawn quadrant of Saturn's magnetosphere, and its relationship to auroral UV and radio emissions. *Planetary and Space Science*, 57 (14–15), 1732-1742, https://doi.org/10.1016/j.pss.2009.04.002.

Müller, A. L., Saur, J., Krupp, N., Roussos, E., Mauk, B. H., Rymer, A. M., Mitchell, D. G., and Krimigis, S. M. (2010), Azimuthal plasma flow in the Kronian magnetosphere, *J. Geophys. Res.*, 115, A08203, doi:10.1029/2009JA015122.

Nichols, J. D., et al. (2014), Dynamic auroral storms on Saturn as observed by the Hubble Space Telescope, *Geophys. Res. Lett.*, 41, 3323– 3330, doi:10.1002/2014GL060186.

1195 Paranicas, C., Mitchell, D. G., Roelof, E. C., Brandt, P. C., Williams, D. J., Krimigis, S. M., and Mauk,
1196 B. H. (2005), Periodic intensity variations in global ENA images of Saturn, *Geophys. Res. Lett.*, 32,
1197 L21101, doi:10.1029/2005GL023656.
1198
1199 Paranicas, C., et al. (2010). Transport of energetic electrons into Saturn's inner magnetosphere. *J.*
1200 *Geophys. Res.*, 115, A09214, doi:10.1029/2010JA015853.
1201
1202 Paranicas, C., Thomsen, M.F., Achilleos, N., Andriopoulou, M., Badman, S. V., Hospodarsky, G., et
1203 al. (2016). Effects of radial motion on interchange injections at Saturn. *Icarus*, 264, 342-351,
1204 https://doi.org/10.1016/j.icarus.2015.10.002.
1205
1206 Pilkington, N. M., Achilleos, N., Arridge, C. S., Guio, P., Masters, A., Ray, L. C., Sergis, N., Thomsen,
1207 M. F., Coates, A. J., and Dougherty, M. K. (2015). Internally driven large-scale changes in the size of
1208 Saturn's magnetosphere. *J. Geophys. Res. Space Physics*, 120, 7289– 7306,
1209 doi:10.1002/2015JA021290.
1210
1211 Provan, G., Andrews, D. J., Arridge, C. S., Coates, A. J., Cowley, S. W. H., Cox, G., et al. (2012). Dual
1212 periodicities in planetary-period magnetic field oscillations in Saturn's tail. *J. Geophys. Res.*, 117,
1213 A01209, doi:10.1029/2011JA017104.
1214
1215 Provan, G., Cowley, S. W. H., Lamy, L., Bunce, E. J., Hunt, G. J., Zarka, P., and Dougherty, M. K.
1216 (2016), Planetary period oscillations in Saturn's magnetosphere: Coalescence and reversal of
1217 northern and southern periods in late northern spring, *J. Geophys. Res. Space Physics*, 121, 9829-
1218 9862, doi:10.1002/2016JA023056.
1219
1220 Radioti, A., Grodent, D., Gérard, J.-C., Roussos, E., Paranicas, C., Bonfond, B., Mitchell, D. G.,
1221 Krupp, N., Krimigis, S., and Clarke, J. T. (2009). Transient auroral features at Saturn: Signatures of
1222 energetic particle injections in the magnetosphere. *J. Geophys. Res.*, 114, A03210,
1223 doi:10.1029/2008JA013632.
1224
1225 Radioti, A., Roussos, E., Grodent, D., Gérard, J.-C., Krupp, N., Mitchell, D. G., Gustin, J., Bonfond, B.,
1226 and Pryor, W. (2013). Signatures of magnetospheric injections in Saturn's aurora. *J. Geophys. Res.*
1227 *Space Physics*, 118, 1922-1933, doi:10.1002/jgra.50161.
1228
1229 Radioti, A., Grodent, D., Gérard, J.-C., Southwood, D. J., Chané, E., Bonfond, B., and Pryor, W.
1230 (2017), Stagnation of Saturn's auroral emission at noon, *J. Geophys. Res. Space Physics*, 122, 6078–
1231 6087, doi:10.1002/2016JA023820.
1232
1233 Reed, J. J., Jackman, C. M., Lamy, L., Kurth, W. S., & Whiter, D. K. (2018). Low-frequency extensions
1234 of the Saturn Kilometric Radiation as a proxy for magnetospheric dynamics. *Journal of Geophysical*
1235 *Research: Space Physics*, 123, 443– 463. https://doi.org/10.1002/2017JA024499.
1236
1237 Roelof, E. C. (1989). Remote sensing of the ring current using energetic neutral atoms. *Advances in*
1238 *Space Research*, 9 (12), 195-203, https://doi.org/10.1016/0273-1177(89)90329-3.
1239
1240 Rymer, A. M., Mauk, B. H., Hill, T.W., André, N., Mitchell, D. G., Paranicas, C., et al. (2009).
1241 Cassini evidence for rapid interchange transport at Saturn. *Planetary and Space Science*, 57 (14–15),
1242 1779-1784, doi:10.1016/j.pss.2009.04.010.
1243
1244 Sergis, N., Krimigis, S. M., Mitchell, D. G., Hamilton, D. C., Krupp, N., Mauk, B. H., Roelof, E. C., and
1245 Dougherty, M. K. (2009). Energetic particle pressure in Saturn's magnetosphere measured with the

Magnetospheric Imaging Instrument on Cassini. *J. Geophys. Res.*, 114, A02214, doi:10.1029/2008JA013774.

Smith, A. W., Jackman, C. M., and Thomsen, M. F. (2016). Magnetic reconnection in Saturn's magnetotail: A comprehensive magnetic field survey. *J. Geophys. Res. Space Physics*, 121, 2984-3005, doi:10.1002/2015JA022005.

Sorba, A. M., Achilleos, N. A., Guio, P., Arridge, C. S., Pilkington, N. M., Masters, A., Sergis, N., Coates, A. J., and Dougherty, M. K. (2017). Modeling the compressibility of Saturn's magnetosphere in response to internal and external influences. *J. Geophys. Res. Space Physics*, 122, 1572– 1589, doi:10.1002/2016JA023544.

Sorba, A. M., Achilleos, N. A., Guio, P., Arridge, C. S., Sergis, N., & Dougherty, M. K. (2018). The periodic flapping and breathing of Saturn's magnetodisk during equinox. *Journal of Geophysical Research: Space Physics*, 123, 8292– 8316. https://doi.org/10.1029/2018JA025764.

Sorba, A. M., Achilleos, N. A., Sergis, N., Guio, P., Arridge, C. S., & Dougherty, M. K. (2019). Local time variation in the large-scale structure of Saturn's magnetosphere. *Journal of Geophysical Research: Space Physics*, 124. https://doi.org/10.1029/2018JA026363.

Southwood, D. J., and Kivelson, M. G. (1989). Magnetospheric interchange motions. *J. Geophys. Res.*, 94 (A1), 299– 308, doi:10.1029/JA094iA01p00299.

Thomsen, M. F., Reisenfeld, D. B., Delapp, D. M., Tokar, R. L., Young, D. T., Crary, F. J., Sittler, E. C., McGraw, M. A., and Williams, J. D. (2010). Survey of ion plasma parameters in Saturn's magnetosphere. *J. Geophys. Res.*, 115, A10220, doi:10.1029/2010JA015267.

Thomsen, M. F. (2013). Saturn's magnetospheric dynamics. *Geophys. Res. Lett.*, 40, 5337– 5344, doi:10.1002/2013GL057967.

Thomsen, M. F., Jackman, C. M., Tokar, R. L., and Wilson, R. J. (2014). Plasma flows in Saturn's nightside magnetosphere. *J. Geophys. Res. Space Physics*, 119, 4521– 4535, doi:10.1002/2014JA019912.

Thomsen, M. F., Mitchell, D. G., Jia, X., Jackman, C. M., Hospodarsky, G., and Coates, A. J. (2015). Plasmapause formation at Saturn. *J. Geophys. Res. Space Physics*, 120, 2571– 2583, doi:10.1002/2015JA021008.

Thomsen, M. F., Jackman, C. M., Cowley, S. W. H., Jia, X., Kivelson, M. G., and Provan, G. (2017). Evidence for periodic variations in the thickness of Saturn's nightside plasma sheet. *J. Geophys. Res. Space Physics*, 122, 280– 292, doi:10.1002/2016JA023368.

Vasyliunas, V. M. (1983). 'Plasma distribution and flow', in *Physics of the Jovian magnetosphere.* (A83-2661 10-91) Cambridge and New York, Cambridge University Press, 1983, 395-453.

Wolf, R. A., Wan, Y., Xing, X., Zhang, J.-C., and Sazykin, S. (2009). Entropy and plasma sheet transport. *J. Geophys. Res.*, 114, A00D05, doi:10.1029/2009JA014044.

Ye, S.-Y., Gurnett, D. A., Fischer, G., Cecconi, B., Menietti, J. D., Kurth, W. S., Wang, Z., Hospodarsky, G. B., Zarka, P., and Lecacheux, A. (2009). Source locations of narrowband radio emissions detected at Saturn. *J. Geophys. Res.*, 114, A06219, doi:10.1029/2008JA013855.

1297
1298 Young, D. T., Berthelier, J.-J., Blanc, M., Burch, J. L., Bolton, S., Coates, A. J., et al. (2005).
1299 Composition and Dynamics of Plasma in Saturn's Magnetosphere. *Science*, 307 (5713), 1262-1266
1300 doi:10.1126/science.1106151.
1301
1302 Zarka, P., Lamy, L., Cecconi, B. et al. (2007). Modulation of Saturn's radio clock by solar wind speed.
1303 *Nature,* 450, 265–267, doi:10.1038/nature06237.

Figure 3.

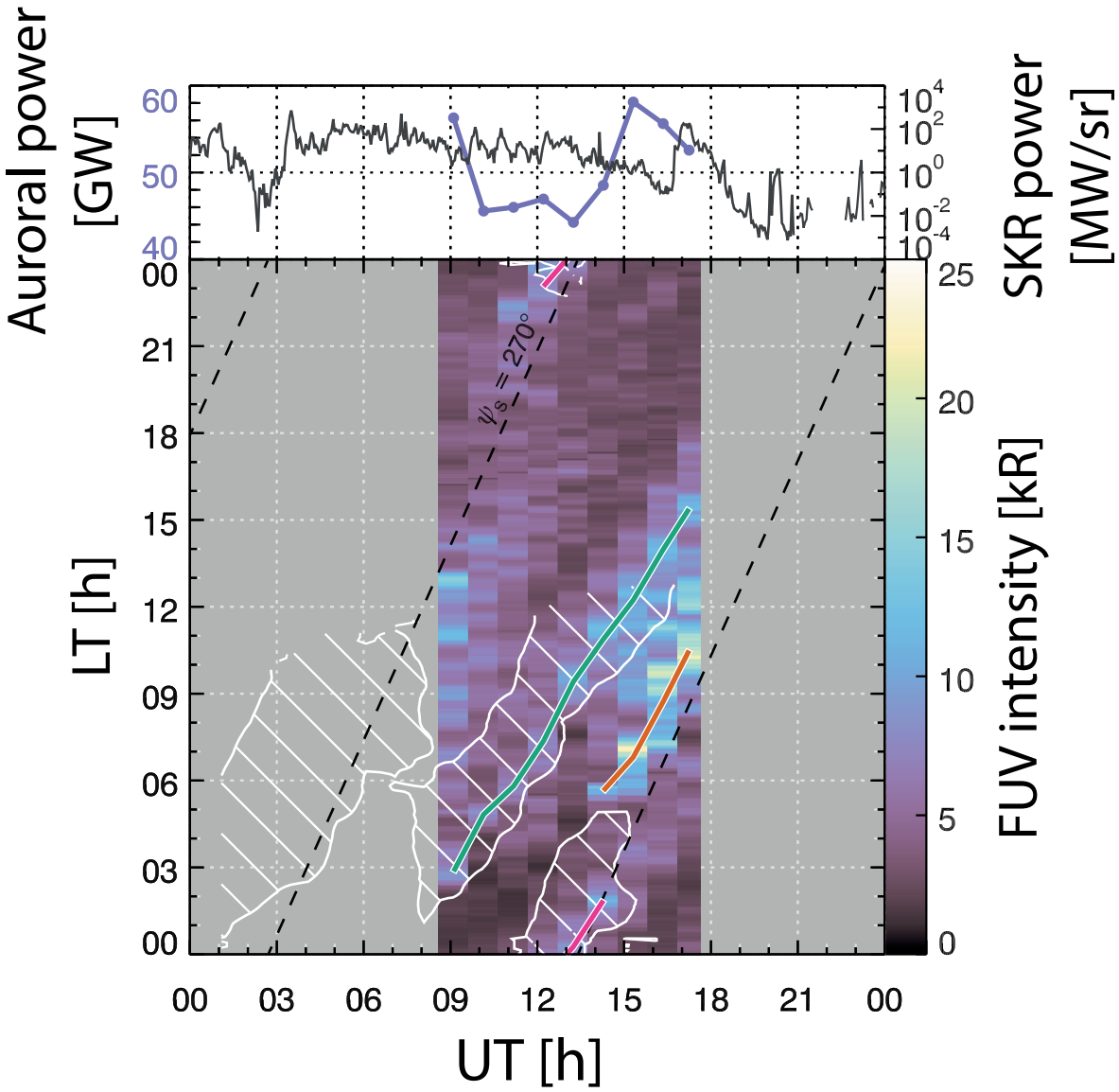
Auroral power
[GW]
60
50
40
SKR power
[MW/sr]
10^4
10^2
10^0
10^{-2}
10^{-4}
$\psi_s = 270°$
LT [h]
00
21
18
15
12
09
06
03
00
FUV intensity [kR]
25
20
15
10
5
0
00
03
06
09
12
15
18
21
00
UT [h]

Figure 1.

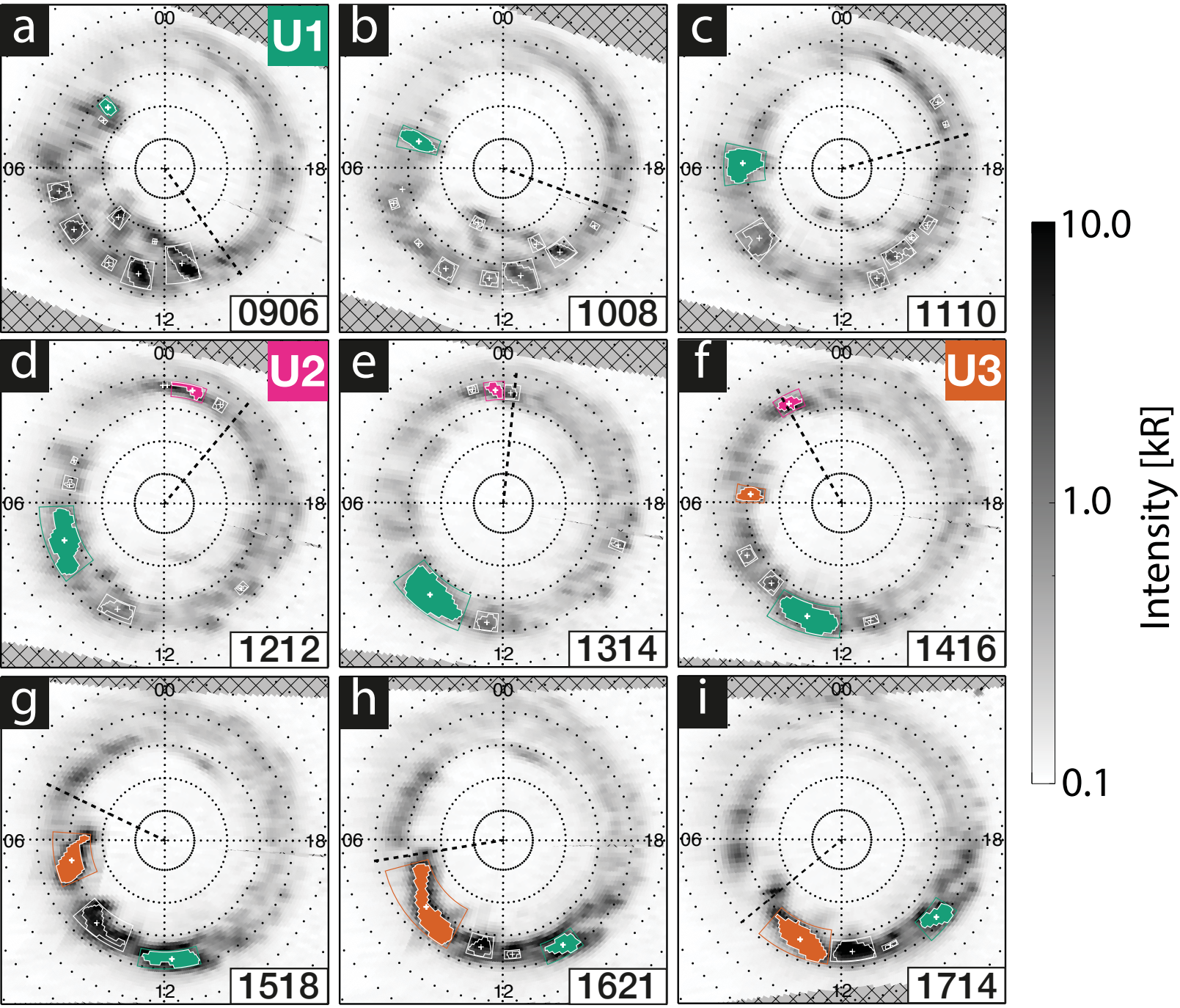
a
U1
b
c
d
U2
e
f
U3
g
h
i
00
06
18
12
0906
1008
1110
1212
1314
1416
1518
1621
1714
10.0
1.0
0.1
Intensity [kR]

Figure 4.

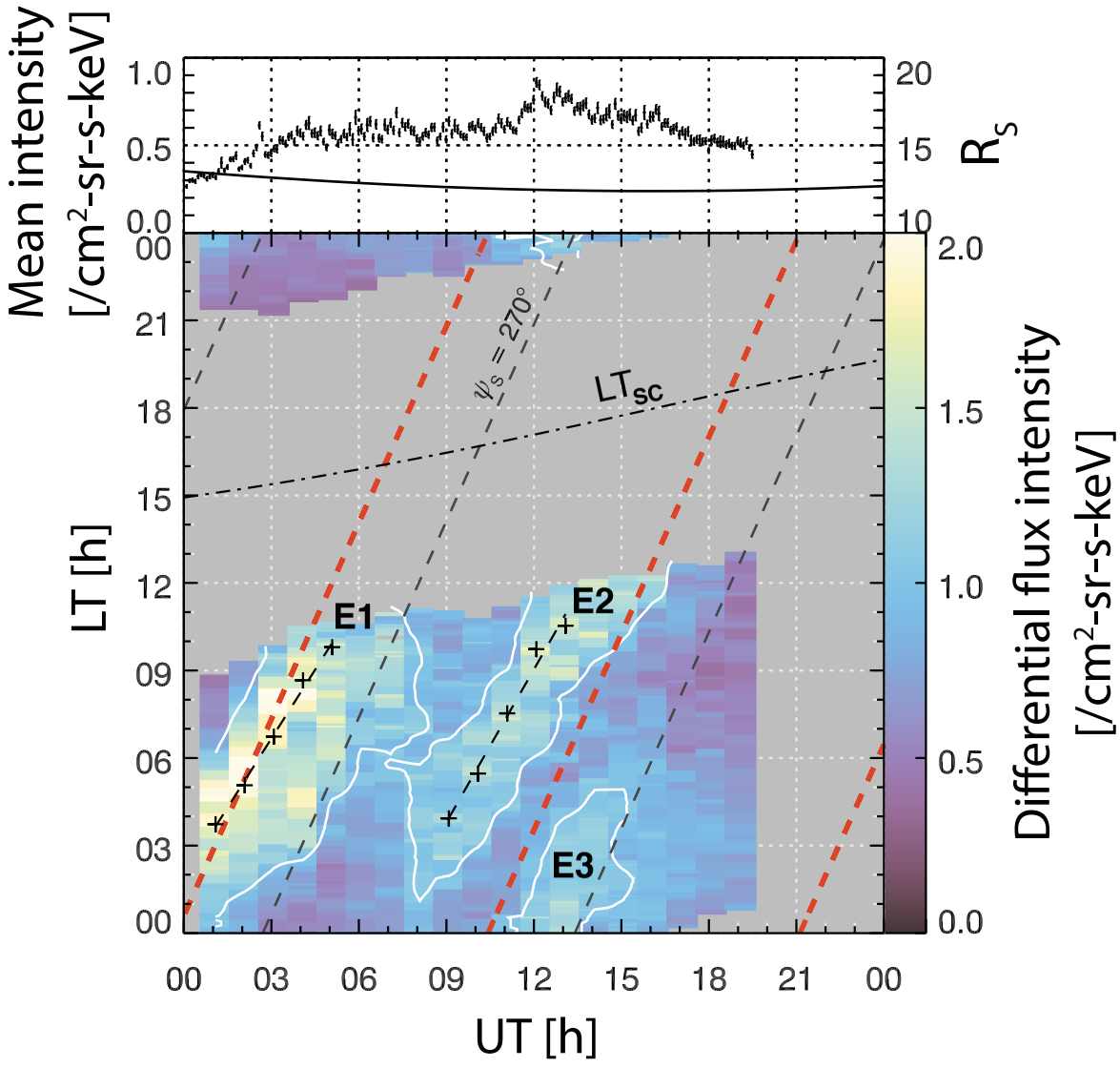
Mean intensity
[/cm²-sr-s-keV]
1.0
0.5
0.0
20
15
10
R_S
00
21
18
15
12
09
06
03
00
LT [h]
$\psi_S = 270°$
LT_{SC}
E1
E2
E3
2.0
1.5
1.0
0.5
0.0
Differential flux intensity
[/cm²-sr-s-keV]
00
03
06
09
12
15
18
21
00
UT [h]

Figure 2.

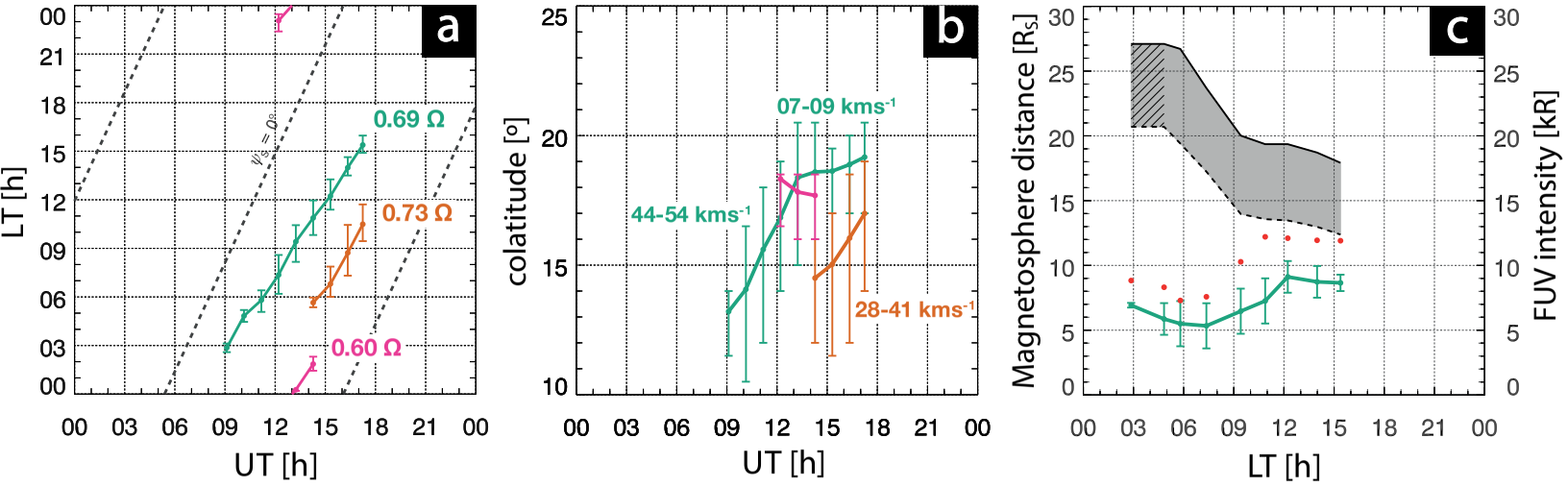
a
b
c
LT [h]
UT [h]
0.69 Ω
0.73 Ω
0.60 Ω
$\psi_S = 0°$
colatitude [°]
07-09 kms^{-1}
44-54 kms^{-1}
28-41 kms^{-1}
Magnetosphere distance [R_S]
FUV intensity [kR]
LT [h]

Figure 5.

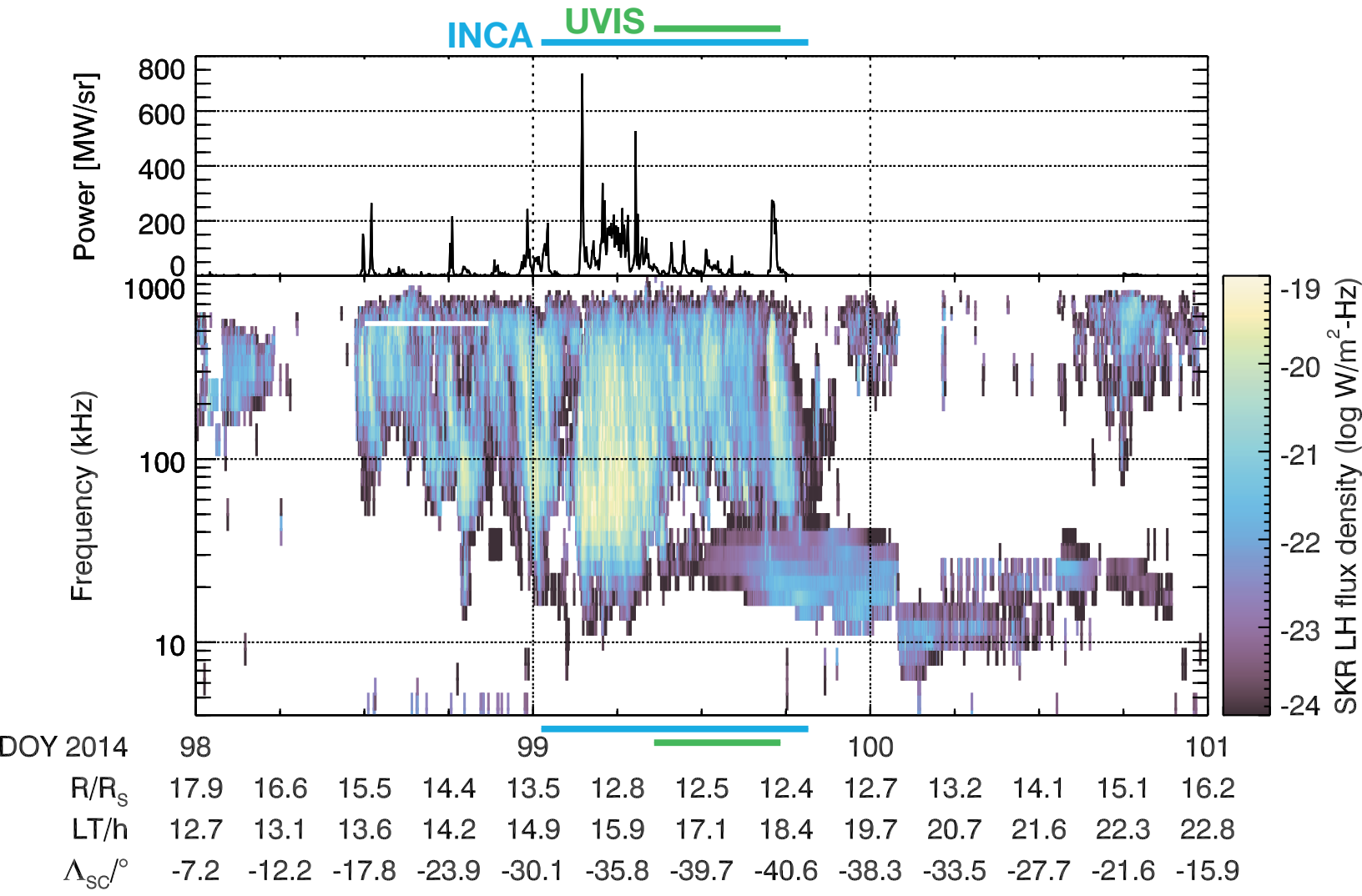
INCA
UVIS
Power [MW/sr]
800
600
400
200
0
Frequency (kHz)
1000
100
10
SKR LH flux density (log W/m^2-Hz)
-19
-20
-21
-22
-23
-24
DOY 2014
98
99
100
101
R/R$_S$
17.9 16.6 15.5 14.4 13.5 12.8 12.5 12.4 12.7 13.2 14.1 15.1 16.2
LT/h
12.7 13.1 13.6 14.2 14.9 15.9 17.1 18.4 19.7 20.7 21.6 22.3 22.8
Λ_{SC}/°
-7.2 -12.2 -17.8 -23.9 -30.1 -35.8 -39.7 -40.6 -38.3 -33.5 -27.7 -21.6 -15.9